

AD-A250 568**DOCUMENTATION PAGE**Form Approved
OMB No. 0704-0188

This form is estimated to average 1 hour per response, including the time for reviewing instructions, searching existing data sources, gathering and maintaining the data needed, and completing and reviewing the collection of information. Send comments regarding this burden estimate or any other aspect of this burden to Washington Headquarters Services, Directorate for Information Operations and Reports, 1215 Jefferson Davis Highway, Suite 1204, Arlington, VA 22202-4302, and to the Office of Management and Budget, Paperwork Reduction Project (0704-0188), Washington, DC 20503.

2. REPORT DATE June 1991		3. REPORT TYPE AND DATES COVERED THESIS/DISSERTATION
4. TITLE AND SUBTITLE Simulation of Diurnally Varying Downslope Winds Over Northern Utah		
5. FUNDING NUMBERS <i>(Handwritten mark)</i>		
6. AUTHOR(S) Kim M. Rigling, Capt		
7. PERFORMING ORGANIZATION NAME(S) AND ADDRESS(ES) AFIT Student Attending: University of Utah		8. PERFORMING ORGANIZATION REPORT NUMBER AFIT/CI/CIA-91-116
9. SPONSORING/MONITORING AGENCY NAME(S) AND ADDRESS(ES) AFIT/CI Wright-Patterson AFB OH 45433-6583		10. SPONSORING / MONITORING AGENCY REPORT NUMBER
11. SUPPLEMENTARY NOTES		
12a. DISTRIBUTION/AVAILABILITY STATEMENT Approved for Public Release IAW 190-1 Distributed Unlimited ERNEST A. HAYGOOD, Captain, USAF Executive Officer		12b. DISTRIBUTION CODE
13. ABSTRACT (Maximum 200 words)		
DISTRIBUTION STATEMENT Approved for public release Distribution Unlimited		
14. SUBJECT TERMS		15. NUMBER OF PAGES 72
16. PRICE CODE		

17. SECURITY CLASSIFICATION OF REPORT	18. SECURITY CLASSIFICATION OF THIS PAGE	19. SECURITY CLASSIFICATION OF ABSTRACT	20. LIMITATION OF ABSTRACT
---------------------------------------	--	---	----------------------------

**SIMULATION OF DIURNALLY VARYING
DOWNSLOPE WINDS OVER
NORTHERN UTAH**

by

Kim Michelle Rigling

A thesis submitted to the faculty of
The University of Utah
in partial fulfillment of the requirements for the degree of

Master of Science

Department of Meteorology

The University of Utah

June 1991

Author: Kim M. Rigling

Title: Simulation of Diurnally Varying Downslope Winds over
Northern Utah

Rank/Service: Captain, USAF

Date: 1991

Number of Pages: 72

Degree: Master of Science, Department of Meteorology

Institution: University of Utah

Accession For	
NTIS GRA&I	<input checked="" type="checkbox"/>
DTIC TAB	<input type="checkbox"/>
Unannounced	<input type="checkbox"/>
Justification	
By _____	
Distribution/ _____	
Availability Code/ _____	
Dist	Avail and/or Special
A-1	

92-11944



92 5 01 028

Copyright © Kim Michelle Rigling 1991

All Rights Reserved

THE UNIVERSITY OF UTAH GRADUATE SCHOOL

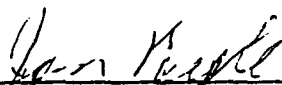
SUPERVISORY COMMITTEE APPROVAL

of a thesis submitted by

Kim Michelle Rigling

This thesis has been read by each member of the following supervisory committee and by majority vote has been found to be satisfactory.

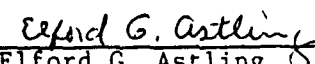
April 12, 1991


Chair: Jan Paegle

April 12, 1991


John Horel

April 12, 1991


Elford G. Astling

THE UNIVERSITY OF UTAH GRADUATE SCHOOL

FINAL READING APPROVAL

To the Graduate Council of the University of Utah:

I have read the thesis of Kim Michelle Rigling in its final form and have found that (1) its format, citations, and bibliographic style are consistent and acceptable; (2) its illustrative materials including figures, tables, and charts are in place; (3) the final manuscript is satisfactory to the Supervisory Committee and is ready for submission to the Graduate School.

May 13, 1991

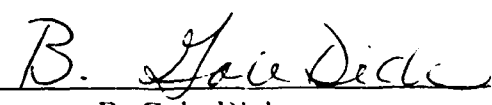
Date


Jan Paegle
Chair, Supervisory Committee

Approved for the Major Department


J.E. Geisler
Chair/Dean

Approved for the Graduate Council


B. Gale Dick
Dean of The Graduate School

ABSTRACT

A relatively complete regional model is utilized to simulate downslope winds in two dimensions. The purpose of this study is to investigate the applicability of conclusions gained by prior investigators using simpler models that lacked diurnal solar cycles and have not explicitly included boundary layer physics. The model used in this study retains turbulent kinetic energy and surface energy budgets as well as longwave and shortwave radiative effects, and is applied to a realistic section of topography over Northern Utah. The diurnal cycle, established by the radiation calculations and reinforced with the prognostic turbulence closure terms, is found to be a first order effect and therefore essential for the evolution of windstorm events. These events are characterized by a nocturnal maximum in the forecast wind fields and development of a strong low level temperature inversion. Winds are weakest in the early afternoon at the time of strongest vertical turbulent mixing and most unstable stratification.

This study confirms previous findings on the importance of the vertical wind and stability profiles to the amplification of downslope winds. It also investigates the dynamics of the momentum equation, and finds that, over most of the region of strong winds, the Bernoulli and dissipation terms oppose the pressure gradient and terrain following terms, and the Coriolis term is negligible.

Preliminary results for the three-dimensional case are presented and appear to validate the results of the two-dimensional case for present goals.

CONTENTS

ABSTRACT	iv
LIST OF FIGURES	vii
ACKNOWLEDGMENTS	xi
 CHAPTERS	
1. INTRODUCTION	1
2. NUMERICAL MODEL	8
2.1 Full Equations	8
2.1.1 Dynamics	8
2.1.2 Physics	10
2.1.3 Numerical Methods	11
2.2 Simplifications Tested	11
2.2.1 Vertical Mixing Coefficient	11
2.2.2 Radiation	12
2.3 Boundary Conditions	12
2.3.1 Top	12
2.3.2 Lateral Sides	12
2.3.3 Sponge Layers	12
2.4 Model Initialization	13
2.5 Domain	13
3. BASIC NUMERICAL EXPERIMENTS	17
3.1 Boundary Placement and Sponge Layer	17
3.2 Resolution	21
3.3 Simplifications Tested	21
3.3.1 Vertical Mixing Coefficient	22
3.3.2 Radiation	27
4. PHYSICAL EXPERIMENTS	32
4.1 Vertical Wind Profiles	32
4.2 Stability	34
4.3 Dynamical Interpretation	42
4.4 Examination of Downstream Wind Profile	46

5. EXPERIMENTS IN THREE DIMENSIONS	48
5.1 Domain and Initialization	48
5.2 Results	48
6. CONCLUSIONS	55
REFERENCES	58

LIST OF FIGURES

2.1 Original topographical input.	14
2.2 Topography after imposition of periodic boundaries.	14
2.3 Terrain after being Fourier filtered.	15
2.4 Final terrain profile after interpolation to 65 grid points.	15
3.1 Vertical cross-section showing location of mountain centered in domain.	18
3.2 Vertical cross-section showing location of mountain offset to east side of domain.	18
3.3 Forecast zonal wind component vs. time, at grid point 15 and a height of 300 m, for the terrain shown in Fig. 3.1. Lower ordinate values indicate stronger easterlies in this and subsequent time plots.	19
3.4 Forecast zonal wind component vs. time, at grid point 23 and a height of 300 m, for the terrain shown in Fig. 3.2.	19
3.5 Forecast zonal wind component vs. time, at grid point 15 and a height of 300 m, for the terrain shown in Fig. 3.1, with sponge layers.	20
3.6 Forecast zonal wind component vs. time, at grid point 23 and a height of 300 m, for the terrain shown in Fig. 3.2, with sponge layers.	20
3.7 Forecast zonal wind component vs. time, for grid point 42 and height of 300 m, for the complete equations.	23
3.8 Vertical cross-section of forecast wind field at midnight local time. Contour interval is 3 m/sec.	23
3.9 Vertical cross-section of potential temperature at midnight local time. Contour interval is 5°K.	24
3.10 Vertical cross-section of potential temperature at noon local time on day two. Contour interval is 5°K.	24
3.11 K_z vs. time for a height of 10 m. Thin line is derived from Eq. (2.6), bold line from Eq. (2.12).	25

3.12 K_z vs. time for a height of 300 m. Thin line is derived from Eq. (2.6), bold line from Eq. (2.12).	25
3.13 Forecast zonal wind component vs. time, for grid point 42 and height of 300 m with simplified K_z	26
3.14 Vertical cross-section of forecast wind field with simplified K_z at midnight local time. Contour interval is 3 m/sec.	26
3.15 Vertical cross-section of potential temperature with simplified K_z at midnight local time. Contour interval is $5^{\circ}K$	28
3.16 Vertical cross-section of potential temperature with simplified K_z at noon local time on day two. Contour interval is $5^{\circ}K$	28
3.17 Forecast zonal wind component vs. time, for grid point 42 and height of 300 m, without radiation terms.	30
3.18 Vertical cross-section of forecast wind field without radiation terms at midnight local time. Contour interval is 3 m/sec.	30
3.19 Vertical cross-section of potential temperature without radiation terms at midnight local time. Contour interval is $5^{\circ}K$	31
3.20 Vertical cross-section of potential temperature without radiation terms at noon local time on day two. Contour interval is $5^{\circ}K$	31
4.1 Initial wind profile for constant wind with height.	33
4.2 Initial wind profile for linearly increasing winds.	33
4.3 Initial wind profile for a reversing wind field.	35
4.4 Forecast zonal wind component vs. time, for grid point 42 at 300 m, using profile shown in Fig. 4.1. Same as Fig. 3.7, but truncated after 24 hours.	35
4.5 Forecast zonal wind component vs. time, for grid point 42 at 300 m, using profile shown in Fig. 4.2.	36
4.6 Forecast zonal wind component vs. time, for grid point 42 at 300 m, using profile shown in Fig. 4.3.	36
4.7 Vertical cross-section of forecast wind field for initial profile shown in Fig. 4.2. at midnight local time. Contour interval is 3 m/sec.	37

4.8 Vertical cross-section of forecast wind field for initial profile shown in Fig. 4.3. at midnight local time. Contour interval is 3 m/sec.	37
4.9 Initial temperature profile for constant stability case.	38
4.10 Initial temperature profile for a surface based inversion.	39
4.11 Initial temperature profile for an inversion based near mountaintop. . .	39
4.12 Forecast zonal wind component vs. time plot, for grid point 42 at 300 m, using profile given in Fig. 4.10.	40
4.13 Forecast zonal wind component vs. time plot, for grid point 42 at 300 m, using profile given in Fig. 4.11.	40
4.14 Vertical cross-section of forecast wind field for initial profile shown in Fig. 4.10. at midnight local time. Contour interval is 3 m/sec. . . .	41
4.15 Vertical cross-section of forecast wind field for initial profile shown in Fig. 4.11. at midnight local time. Contour interval is 3 m/sec. . . .	41
4.16 Coriolis contribution of Eq. (4.4). Contour interval is .005 m/sec ²	43
4.17 Bernoulli contribution of Eq. (4.4). Contour interval is .005 m/sec ²	43
4.18 Pressure gradient contribution of Eq. (4.4). Contour interval is .005 m/sec ²	44
4.19 Terrain contribution of Eq. (4.4). Contour interval is .005 m/sec ²	44
4.20 Local acceleration term of Eq. (4.4). Contour interval is .005 m/sec ² . .	45
4.21 Residual for Eq. (4.4). Contour interval is .005 m/sec ²	45
4.22 Wind amplification vs. grid point at a height of 10 m.	47
5.1 Terrain for three-dimensional run. Contour interval is 100 m.	49
5.2 Forecast u wind component vs. time plot for point I=20, J=10, at a height of 300 m.	50
5.3 Horizontal map of forecast winds at a height of 10 m. Contour interval is 3 m/sec.	50
5.4 Horizontal map of forecast wind field at a height of 300 m. Contour interval is 3 m/sec.	51

5.5	Horizontal map of forecast vector winds at a height of 300 m. Contour interval for topography is 100 m.	51
5.6	Terrain profile at J=7.	52
5.7	East-west vertical cross-section of forecast wind field at J=7. Contour interval is 3 m/sec.	52
5.8	Terrain profile at J=10.	53
5.9	East-west vertical cross-section of forecast wind field at J=10. Contour interval is 3 m/sec.	53

ACKNOWLEDGMENTS

This research and thesis were made possible by the advice and encouragement of my advisor, Dr. Jan Paegle, and the support of the U. S. Air Force, through the Air Force Institute of Technology (AFIT). Many helpful suggestions were also made by Dr. John Horel and Dr. Elford Astling.

Special thanks also to my fellow student and friend, Steve Gilbert, for his help and moral support.

Finally, thanks to my family for always being there for me.

CHAPTER 1

INTRODUCTION

The study of dynamical aspects of downslope windstorms has a relatively long history. Experimental results by Long (1953, 1955) are the basis of much of the current knowledge in the field of stratified fluid flow. An excellent review of Long's work, observational studies by Förchtgott (1949, 1952), as well as some early theoretical studies, including those by Queney (1947) and Scorer (1949, 1953, 1954), are summarized in a review article by Corby (1954). Corby recognized the importance of Scorer's inclusion of the effects of vertical variation of the stability and wind shear. The numerical relationship of these terms has come to be known as the Scorer number and is expressed as:

$$S = \frac{1}{k^2} \left(\frac{g\beta}{U^2} - \frac{1}{U} \frac{\partial^2 U}{\partial z^2} \right) \quad (1.1)$$

where k is the zonal wave number of the disturbance, g is gravity, β is a measure of stability, and U is the horizontal wind velocity.

This number was the basis for one of the first theories of downslope winds to gain widespread acceptance; the *trapped lee wave* theory of Scorer and Klieforth (1959). Trapped lee waves occur when the wind profile exhibits a rapid increase in speed with increasing height which prevents the upward propagation of the wave energy. The numerical relationship of the stability and wind shear terms, as expressed by the Scorer number, are still widely accepted; however, trapped lee waves are no longer thought to be a mechanism by which strong downslope windstorms develop.

Observations have indicated that waves associated with strong windstorms have a longer horizontal wavelength than that predicted by trapped lee wave theory and do propagate vertically. Several new theories were proposed during the 1970s. Three mechanisms that will be discussed briefly are the *resonant lee wave theory*, the *wave breaking theory* and the *hydraulic jump theory*.

Klemp and Lilly (1975, 1978) suggested that the mechanism is one of resonant lee waves, which differs from the trapped lee wave theory in that the waves are free to propagate vertically. The waves are partially reflected downward by stability variations and strong winds result from an optimal superposition of the upward and downward propagating components. Klemp and Lilly (1975) used a two-dimensional, linear, hydrostatic, steady-state model with potential temperature as a vertical coordinate to model the 11 January 1972 windstorm near Boulder, Colorado. This windstorm has been studied and modeled by several researchers because of the excellent data set available for verification, as discussed in Lilly and Zipser (1972), including aircraft observations and surface anemometer traces taken in Boulder. Their model results appeared to corroborate their analytic conclusions that development of strong winds is greatly influenced by the previously discussed stratification, and that the ideal wind and stability profiles are those which cause the waves to approximately reverse phase between the surface and the tropopause.

Clark and Peltier (1977, 1984) and Peltier and Clark (1979, 1980) argue that the large amplitude waves and downslope winds develop only after wave breaking. They contend that nonlinear waves are reflected by a wave-induced critical level and thus grow by resonance. Their model, described by Clark (1977), is three-dimensional, nonhydrostatic, anelastic and uses a terrain following coordinate system. They used this model to produce an excellent simulation of the resultant horizontal windfield for the 11 January 1972 windstorm. In doing so, they contended that the isentropic coordinate system used by Lilly and Klemp was inappropriate since a local

region of superadiabatic temperature gradient was produced during formation of the wave-induced critical level. Furthermore, use of the hydrostatic approximation was invalid because observations indicated support for strong lee waves, which are nonhydrostatic phenomena.

Lilly and Klemp (1980, p. 2121) defended the relative simplicity of their model. They claimed that although the nonhydrostatic and nonlinear processes are significant, linear theory can predict strong responses from appropriate initial conditions. They recognized the usefulness of more complex models while stating, "there is also merit in exploiting the simplest models which contain the physical core of the problem and also make verifiable predictions."

Finally, the hydraulic jump theory was advanced by Houghton and Isaacson (1968) and Houghton and Kasahara (1968). The principles are based on Long's work, and contend that when a vertically bounded fluid travels up and over an obstacle a hydraulic jump occurs as the flow accelerates from subcritical to supercritical speeds. This mechanism is nonlinear and nonhydrostatic. Durran (1986) applied this theory, using a nonhydrostatic, compressible model with a terrain following coordinate system, to study the 11 January 1972 event. He did simulations comparing the relative importance of the presence of an elevated inversion and changing the stability and wind profiles in the stratosphere. Durran concluded that the elevated inversion was essential to strong wind amplification, while altering the stratospheric profile prevented wave breaking without eliminating the strong winds.

A significant drawback of the hydraulic jump theory is the requirement of an upper boundary, which is either a free surface or rigid plate. This requirement may be more restrictive than many of the assumptions made in other models, such as the hydrostatic approximation.

Subsequent articles continued to examine and compare these theories. Blumen and Hartsough (1985) evaluated the Klemp and Lilly (1975) model using a con-

tinuous versus layered atmospheric profile. Their findings supported Klemp and Lilly's results. Smith (1985, 1987) agrees with Clark and Peltier's conclusions on the importance of wave-breaking; however, he presented a different mathematical basis for amplification. Smith used Long's equation and developed a relationship that explicitly related wave-breaking amplification to mountain height. Clark and Peltier based their model on the physical assumption that a critical level is formed by the wave-overturning, and that this critical level acts as a free-surface to reflect incoming waves. The formation of the critical level can be influenced by terrain height, but the dependence is only implicit.

Although the importance of the elevated inversion is widely accepted, many other factors are still disputed. Clark and Peltier (1984) and Smith (1985) discuss effects of a reversing wind profile, concluding that it may enhance wave-breaking, and thus wind amplification. Durran (1990) suggests that there is not one unique mechanism responsible for all strong wind events. Instead criteria such as the mountain height, mean state flow, and the Brunt-Väisälä frequency all play a role in determining whether, and by which mechanism, a strong windstorm can develop.

The above summary indicates a long and continuing history of theoretical studies of downslope windstorms, which support a variety of dynamical mechanisms. The relative influences of physical mechanisms that actually modulate the evolution of these storms has, however, been less well studied. In particular, the role of the diurnal cycle of surface heating may be expected to modulate downslope windstorms strongly in view of the effect of diurnal cycles upon the low level stratification, a key parameter in the dynamical theories. None of the above cited studies has included realistic diurnal cycles. Similarly, although several studies used first order diagnostic simulations of eddy turbulence, none has allowed a predicted evolution of turbulence. Since a parcel moving through the windstorm experiences rapid local changes of stability and shear, it is more appropriate to allow advective and

temporal changes in the turbulence. First order treatments describe both vertical and horizontal mixing entirely in terms of local shear and stability and do not allow such effects. Finally, most studies have assumed relatively idealized topographic profiles, and many have focused upon atmospheric conditions and verification for cases near Boulder, CO. Consequently, the applicability of the theories to more complex topography and other regions has not been thoroughly tested.

The central goal of this study is to remove some of these simplifications by using realistic local topography of northern Utah, and a model that retains a prognostic turbulence treatment for vertical mixing. Early versions of this model are described by Paegle and McLawhorn (1983), and implementations of real data predictions are contained in studies by Astling et al. (1985) and McCorcle (1986) east of the Rockies, by Paegle et al. (1984) and Paegle and Vukicevic (1987) around the Alps, and by Berri and Paegle (1990) over the Andes. Each of these studies focused upon the boundary layer evolution, and several provided comparisons with observed atmospheric evolution, and thereby validated the physical parameterizations of the model. Recent enhancements of the model now permit execution of deep versions extending through the troposphere, and allow initialization with arbitrarily specified initial conditions on pressure levels. These enhancements allow model applications to the downslope wind problem, and the careful treatments of solar cycles, long wave radiation, and vertical mixing permit more complete explorations of the sensitivity of windstorms to ambient conditions than has been possible with simpler models.

The model has two major assumptions: it is hydrostatic and does not include cloud processes. Scale analysis demonstrates that the hydrostatic assumption is valid whenever the squared ratio of the vertical to horizontal scales is much less than one. This condition holds in most of our integrations, in which the vertical scale of the downslope winds is on the order of 1 km, while the horizontal grid does

not effectively resolve structures much shorter than approximately 10 km.

The version of the model used here does not include moisture, except in the longwave radiation terms. Durran and Klemp (1983, p. 2341) concluded "the addition of moisture to the upstream flow greatly reduces the wave response." Observations during downslope windstorms along the Wasatch front support the conclusion that they are primarily dry events. Thus the lack of moisture and cloud interactions are not significant concerns for the phenomena investigated.

This study is intended to relate some of the factors discussed, such as vertical wind profile and stability, to strong windstorm development over the complex terrain found along the Wasatch Mountains near Salt Lake City, Utah. Another goal is to investigate which characteristics are essential for a model to fully predict strong winds and to distinguish strong windstorms from nonevents. Our interest is due to both the close proximity to the phenomena and the applications of earlier knowledge to other mountain ranges.

The model is described in more detail in Chapter 2 of this thesis. All regional models include artificial lateral boundary conditions. Tests of these conditions are presented in Chapter 3. Both the presence of the radiation calculations and complete parameterization of the vertical mixing coefficient were found to create and enhance the diurnal cycle, thus strengthening the resultant wind fields. These results and the effects of changing the grid size are also found in Chapter 3.

In Chapter 4, sensitivity experiments are presented. They include effects from changing the vertical wind and initial stability profiles, along with analysis of the momentum equation terms to determine the primary forcing mechanism, and the structure of the downstream wind profile.

The results presented in Chapters 3 and 4 were done in two dimensions, as has been the case for much of the work in previous studies. In Chapter 5, some

preliminary results for three-dimensional tests are discussed, while the conclusions are presented in Chapter 6.

CHAPTER 2

NUMERICAL MODEL

2.1 Full Equations

This study uses a version of the regional model described in Paegle and McLawhorn (1983). The atmosphere is modeled to a depth of 10 km, with 17 grid points. The bottom grid point is at the roughness height of .05 m and is constrained to be equal to the top soil level. Variable vertical resolution is used, with the height for each grid point given in Table 2.1. There are 17 soil layers, equally spaced below the surface, to a depth of .64 m. The temperature is calculated for each of these layers to allow storage and retransmission of heat fluxes; however, the soil parameters of heat capacity and density are held constant throughout these experiments.

2.1.1 Dynamics

The model is hydrostatic and utilizes terrain following coordinates. The momentum equations are:

$$\frac{\partial u}{\partial t} + u \frac{\partial u}{\partial x} + v \frac{\partial u}{\partial y} + w \frac{\partial u}{\partial z} - fv = -\frac{1}{\rho_s} \frac{\partial p'}{\partial x} - \frac{\rho'}{\rho_s} g \frac{\partial Z_T}{\partial x} + F_x \quad (2.1)$$

$$\frac{\partial v}{\partial t} + u \frac{\partial v}{\partial x} + v \frac{\partial v}{\partial y} + w \frac{\partial v}{\partial z} + fu = -\frac{1}{\rho_s} \frac{\partial p'}{\partial y} - \frac{\rho'}{\rho_s} g \frac{\partial Z_T}{\partial y} + F_v \quad (2.2)$$

$$\frac{\partial p'}{\partial z} = -\rho' g, \quad (2.3)$$

where (u , v , w) are (eastward, northward, upward) wind components, (x , y , z , t) are the three Cartesian coordinates and time, f is the Coriolis parameter, ρ_s ,

Table 2.1. Vertical grid levels.

Grid point number	height
1	.05 m
2	.1 m
3	1 m
4	10 m
5	100 m
6	300 m
7	500 m
8	1 km
9	2 km
10	3 km
11	4 km
12	5 km
13	6 km
14	7 km
15	8 km
16	9 km
17	10 km

is basic state density, p' is perturbation pressure, ρ' is perturbation density, g is gravitational acceleration, Z_T is terrain height and (F_x, F_y) are frictional forces. The latter are specified by a mixing coefficient treatment and the coefficient (D_k) is proportional to deformation rate.

The anelastic form of the continuity equation is:

$$w \frac{\partial \ln \rho}{\partial z} = - \left[\frac{\partial w}{\partial z} + \left(\frac{\partial u}{\partial x} + \frac{\partial v}{\partial y} \right) \right], \quad (2.4)$$

where ρ is total density.

The atmospheric thermodynamic equation is of the form:

$$\frac{\partial \theta}{\partial t} + u \frac{\partial \theta}{\partial x} + v \frac{\partial \theta}{\partial y} + w \frac{\partial \theta}{\partial z} = \frac{\partial}{\partial z} \left(K_z \frac{\partial \theta}{\partial z} \right) + \text{heating terms}, \quad (2.5)$$

where θ is potential temperature and K_z is turbulent conductivity. Paegle and McLawhorn (1983) give detailed derivations of (2.1) - (2.5).

2.1.2 Physics

The solar angle is computed at each grid point as a function of time of day, day of year and position on the earth's surface. The solar radiation is a function of the albedo and solar angle. Full equations are given in Paegle and McLawhorn (1983). For all of the runs discussed in this thesis, the day of year was taken as 79.2, which corresponds to the vernal equinox. Solar radiation terms specify the incoming radiation, absorption, and reflection with an albedo that was assumed to be constant at 0.3.

The longwave radiation budget is calculated from the upward and downward radiative fluxes from both the atmosphere and surface. Cloud interactions are not included in this version of the model, and water vapor is the only radiative gas considered in the atmospheric calculations. The radiative flux calculations are carried to a height of 12 km above the surface.

The turbulence closure specifies the vertical mixing coefficient by:

$$K_z = \sqrt{2b} l S. \quad (2.6)$$

Here b , the turbulent kinetic energy is forecast by:

$$\begin{aligned} \frac{\partial b}{\partial t} + u \frac{\partial b}{\partial x} + v \frac{\partial b}{\partial y} + w \frac{\partial b}{\partial z} &= K_z \left[\left(\frac{\partial u}{\partial z} \right)^2 + \left(\frac{\partial v}{\partial z} \right)^2 \right] - \frac{g}{T} K_z \frac{\partial \theta}{\partial z} \\ &\quad - \frac{K_z^3}{c(l^4)} + \frac{\partial}{\partial z} \left(K_z \frac{\partial b}{\partial z} \right), \end{aligned} \quad (2.7)$$

where T is temperature. The mixing length, l , is calculated from:

$$l = kz \left[\frac{kz}{\lambda} + \Phi_m \left(\frac{z}{L} \right) \right]^{-1}, \quad (2.8)$$

where k is Von Kàrmàn's constant and the profile functions $\Phi_m(z/L)$ are those used by Zdunkowski et al. (1976). The Monin-Obukhov length scale L is calculated from surface layer gradients, and λ is the height weighted integral of b :

$$\lambda = 1.4 \frac{\int_0^2 \frac{K_m}{b_z dz}}{\int_0^2 \frac{K_m}{b dz}}. \quad (2.9)$$

S is a function of the local Richardson number, (Ri) and the constant a :

$$S = 1.7 \frac{(.213 - \frac{Ri}{a}) (.269 - \frac{Ri}{a})}{(1 - \frac{Ri}{a}) (.25 - \frac{Ri}{a})}. \quad (2.10)$$

We set $a = 1.2$ and S is constrained to be greater than or equal to 0.1. This parameterization is similar to that used by Yamada and Bunker (1989).

2.1.3 Numerical Methods

Eqs. (2.1) - (2.5) are solved by finite difference methods in the horizontal plane and finite element methods in the vertical. The turbulence and diffusion terms are calculated through a backward differencing scheme and thus are fully implicit. Computational modes develop because the scheme is not staggered in space. These are controlled by passing the changes in the horizontal wind components through a Fourier filter. The time step is limited by the Courant-Friedrichs-Lowy stability criterion applied to two space dimensions:

$$\left| \frac{C \Delta t}{\Delta x} \right| \leq .7, \quad (2.11)$$

where C is the maximum horizontal propagation speed. All vertical fluxes are computed with absolutely stable implicit methods.

2.2 Simplifications Tested

2.2.1 Vertical Mixing Coefficient

In the full model equations, the vertical mixing coefficient is that given in the previous section. Tests were also done with this parameterization replaced by a linear function of height through 300 m and constant above, i.e.,

$$K_z = 0.1z, \text{ if } z \leq 300 \text{ and } K_z = 30, \text{ if } z > 300. \quad (2.12)$$

2.2.2 Radiation

The radiation calculations are performed every five minutes to allow interactions between the radiation terms and atmospheric variables which establish a diurnal cycle. Runs were made neglecting the solar and longwave radiation terms to test their importance.

2.3 Boundary Conditions

2.3.1 Top

The initial pressure is maintained and geostrophic flow is assumed at the upper boundary. The hydrostatic equation is used to integrate the pressure downward, from the model top.

2.3.2 Lateral Sides

Initial values of the u and v wind components and temperature are maintained on the boundaries through time (Dirichlet boundary conditions). The boundary values for moisture and turbulent kinetic energy are determined by setting them equal to the values calculated at one grid point within the boundary. This is known as Neumann boundary conditions. A Fourier filter is used to remove waves possessing wavelengths between $2\Delta X$ and $4\Delta X$ to control the growth of computational modes. This filter is applied only on the change from the initial state; thus only the changes must be periodic.

2.3.3 Sponge Layers

The horizontal diffusion coefficient (D_k) is calculated as a function of velocity gradient and grid size. A "sponge" layer was added adjacent to the east and west

boundaries, where horizontal diffusion increases linearly from this interior value to a maximum determined by the grid size and time step. The maximum value is:

$$D_k = \frac{1}{4} \frac{\Delta x^2}{\Delta t}. \quad (2.13)$$

2.4 Model Initialization

The method used throughout these experiments is to initialize from a column of data, provided at selected pressure levels, and interpolate to the model grid. This method allows for variations in the initial stability and vertical wind profile. The initial field is horizontally uniform.

2.5 Domain

The terrain was obtained from a real terrain data set for the Wasatch Mountains, from 112.8 to 110.8 °W, averaged over latitudes 41.0 to 41.1 °N. The area studied comprises the western slopes of the Wasatch Range, where strong easterly winds are sometimes observed. Therefore upstream refers to east of the mountain and downstream to the west.

The data set has 120 grid points per degree longitude and latitude. The initial terrain profile for this 2 ° longitudinal cut is shown in Fig. 2.1. The upstream region was brought back down to a baseline of 1250 m for mass continuity considerations. (Fig. 2.2). This profile was then passed through a Fourier filter consistent with that used for the model equations (Fig. 2.3). These points were interpolated to 33 grid points and finally the downstream plain was smoothed and extended to study the windflow further from the mountains (Fig. 2.4).

The result of these manipulations is a field with 65 grid points in the east-west with a grid size of approximately 5.75 km. This grid size is small enough to model

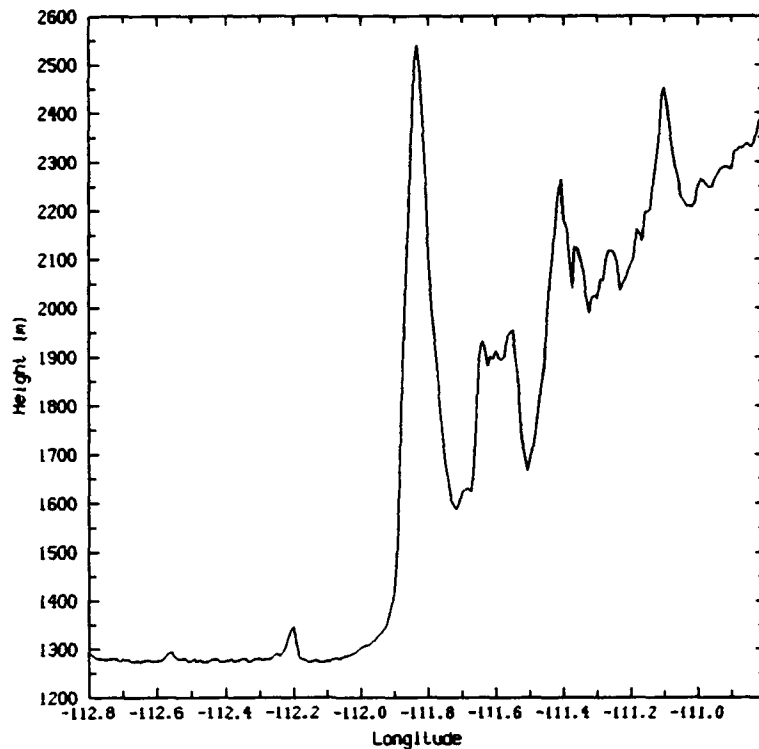


Figure 2.1. Original topographical input.

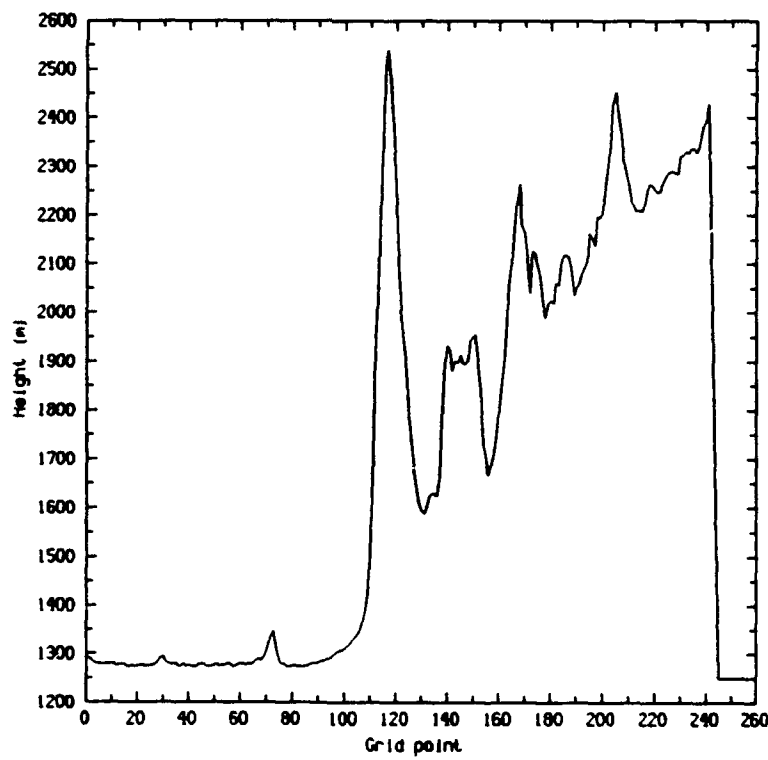


Figure 2.2. Topography after imposition of periodic boundaries.

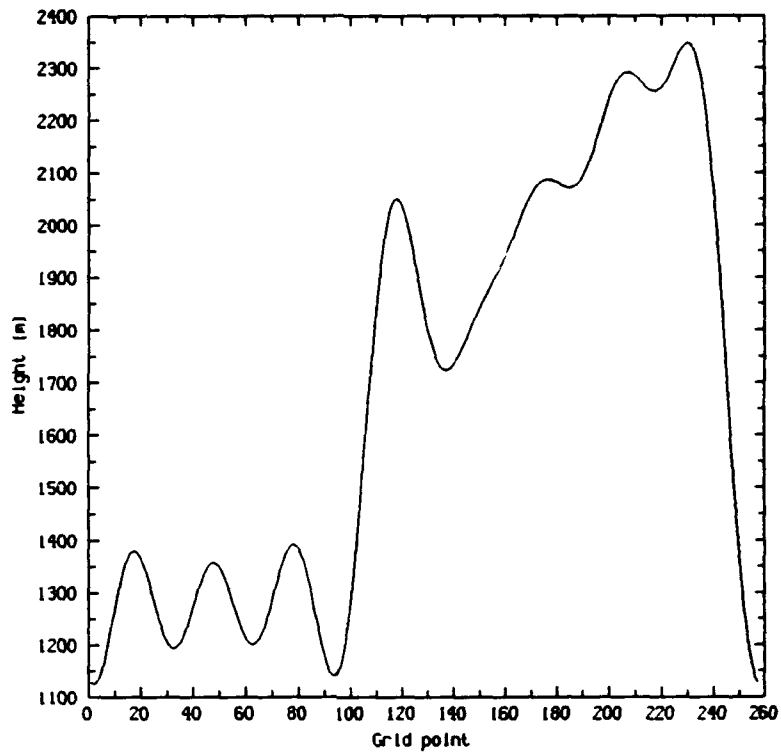


Figure 2.3. Terrain after being Fourier filtered.

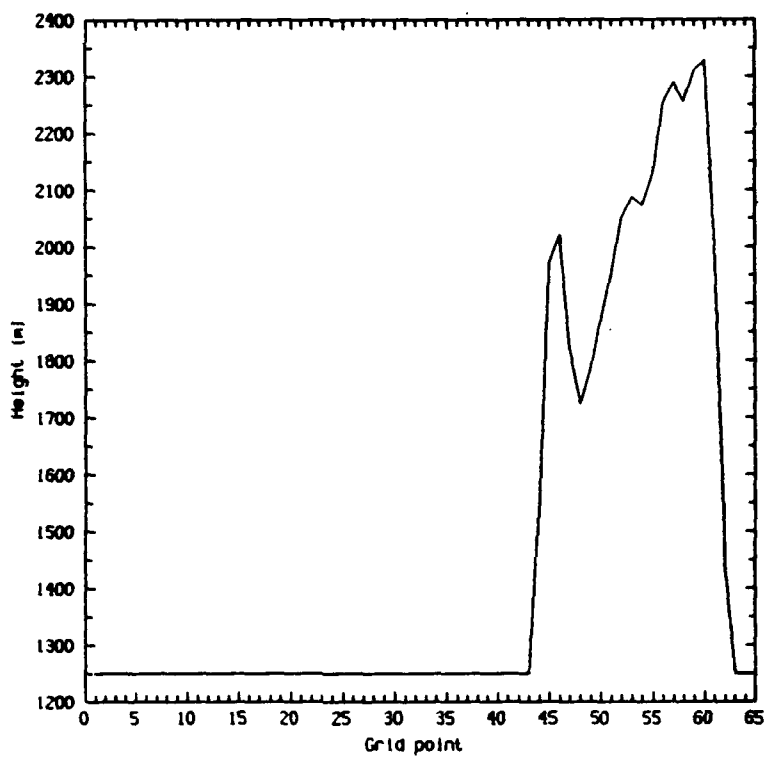


Figure 2.4. Final terrain profile after interpolation to 65 grid points.

steep and complex terrain, but large enough for hydrostatic scale considerations to remain valid.

CHAPTER 3

BASIC NUMERICAL EXPERIMENTS

3.1 Boundary Placement and Sponge Layer

A series of two-dimensional runs with Gaussian terrain, and without radiation terms, demonstrated that the forecasts were dependent on the location of the mountain relative to the domain boundaries. Two mountain positions were tested, one in the middle of the domain (Fig. 3.1) and the other closer to the eastern boundary (Fig. 3.2). Amplifying oscillations appear after about 8 hours in both cases, and these are more pronounced for the topography of Fig. 3.2. Figs. 3.3 and 3.4 show plots of the forecast zonal wind component versus time at a height of 300 m and horizontal grid points 15 and 23, respectively, plotted at each time step. The easterly component is shown as a negative velocity. These oscillations are damped in the runs with sponge layers (Figs. 3.5 and 3.6). The resultant wind field appears to reach a steady-state near 45 m/sec. This is quite strong, but is attributed to the height of the mountain (2400 m). Running the model with the mountain height at 1000 m (not shown) resulted in peak windspeeds of 24 m/sec. The speeds and vertical structure for this run are very comparable to Durran's (1986, Fig. 17) results.

An upper sponge layer was also tested. It was constructed similar to the lateral sponge layers, with an increase in the vertical mixing coefficient near the upper boundary. The boundary value was calculated by:

$$K_z = \frac{1}{4} \frac{\Delta z^2}{\Delta t}. \quad (3.1)$$

This was found to have little effect on the resultant wind fields and so was not used.

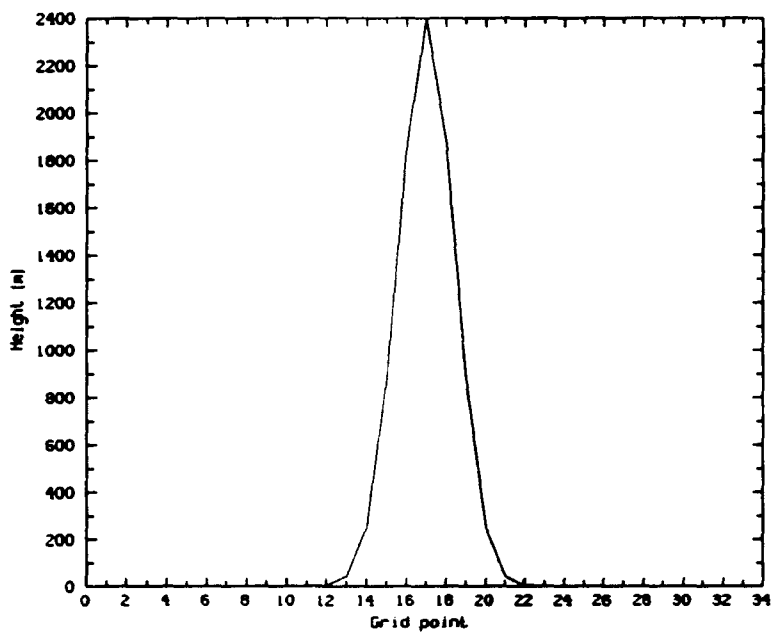


Figure 3.1. Vertical cross-section showing location of mountain centered in domain.

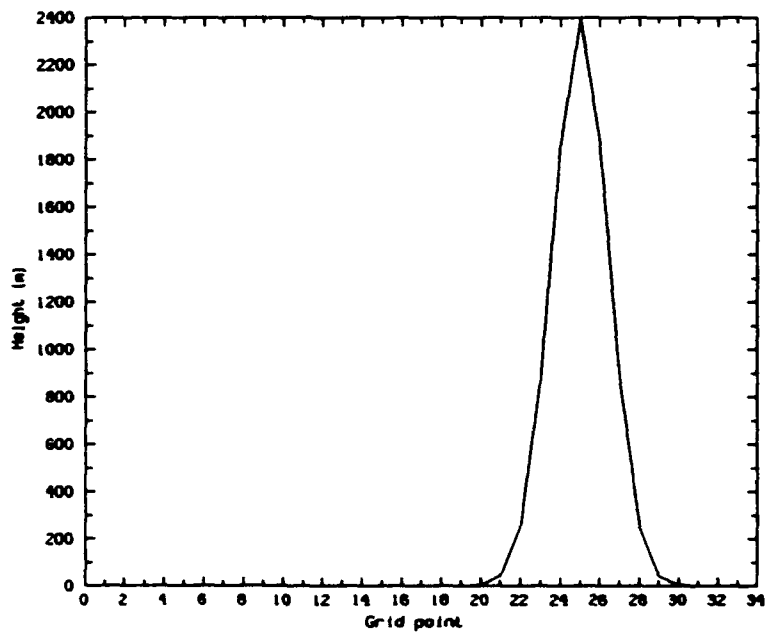


Figure 3.2. Vertical cross-section showing location of mountain offset to east side of domain.

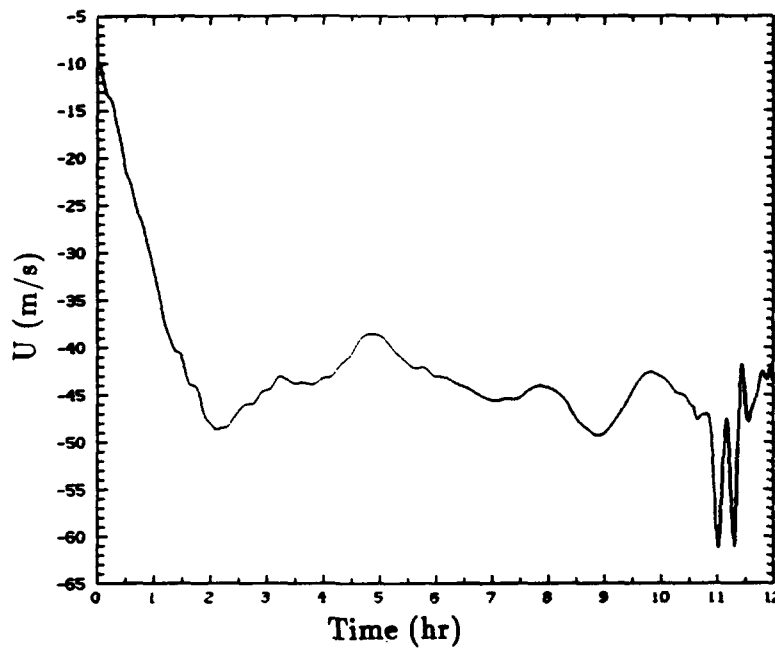


Figure 3.3. Forecast zonal wind component vs. time, at grid point 15 and a height of 300 m, for the terrain shown in Fig. 3.1. Lower ordinate values indicate stronger easterlies in this and subsequent time plots.

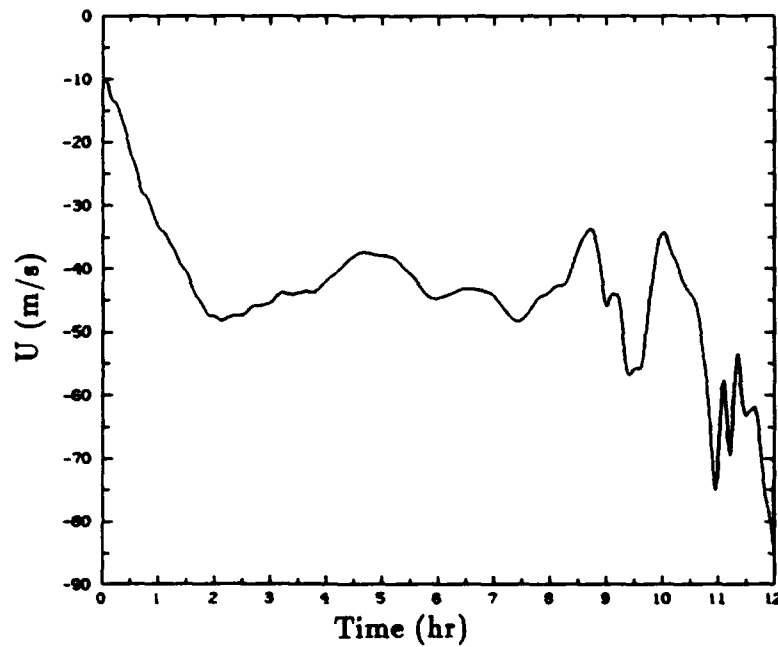


Figure 3.4. Forecast zonal wind component vs. time, at grid point 23 and a height of 300 m, for the terrain shown in Fig. 3.2.

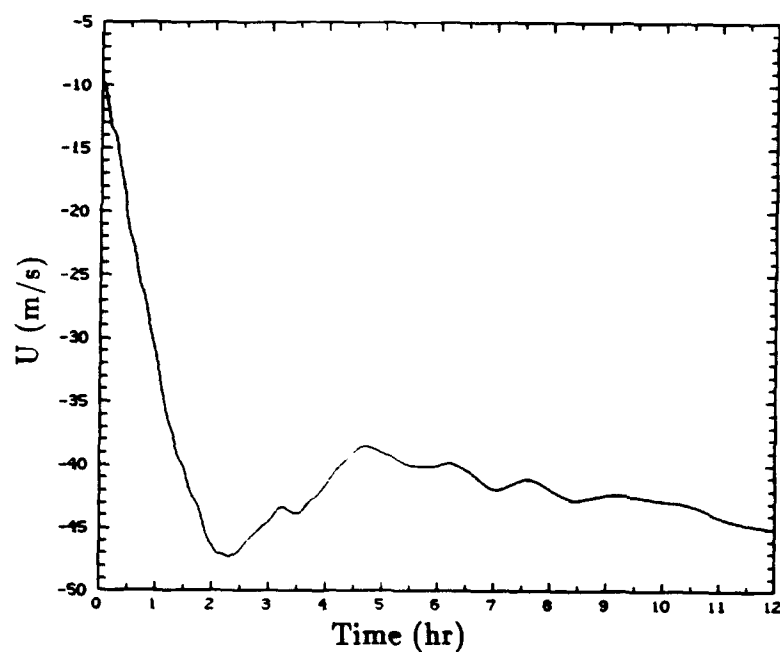


Figure 3.5. Forecast zonal wind component vs. time, at grid point 15 and a height of 300 m, for the terrain shown in Fig. 3.1, with sponge layers.

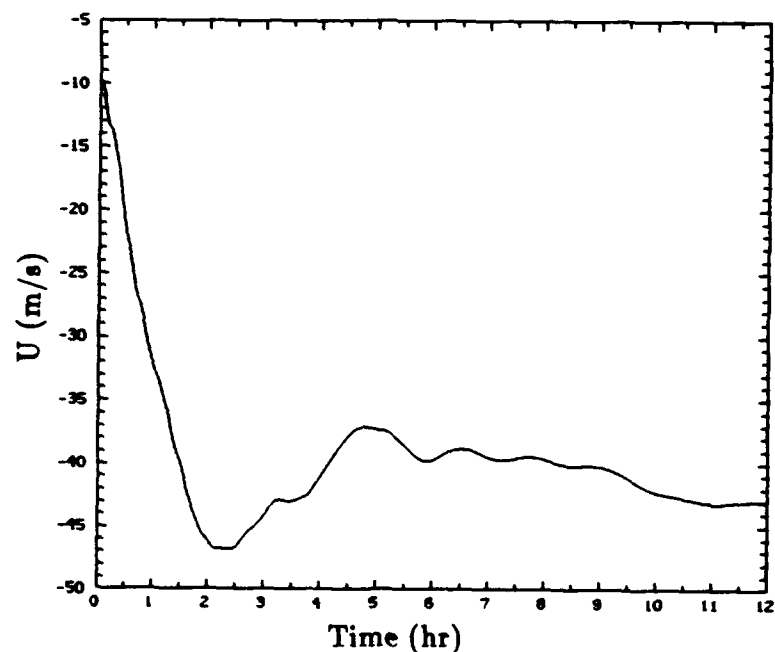


Figure 3.6. Forecast zonal wind component vs. time, at grid point 23 and a height of 300 m, for the terrain shown in Fig. 3.2, with sponge layers.

3.2 Resolution

The effect of varying resolution was tested in early runs with both Gaussian topography and a more realistic terrain cross-section. Using Gaussian topography, the finer resolution runs produced slightly stronger wind fields (not shown), although the pattern was the same. If the grid size was decreased below 5 km, little additional change was apparent. Because of this and the hydrostatic constraint, all subsequent integrations are done with a grid size of 5.7 km, unless otherwise noted.

In the runs with realistic terrain, the results were dependent on the profiles used. Interpolation to a coarse grid led, in some cases, to a markedly different terrain pattern as some peaks or valleys were not resolved. Thus the appropriate scale was dependent on the terrain.

3.3 Simplifications Tested

A control run was done to establish a baseline response to the full forcing of the model in two dimensions, with the terrain given in Fig. 2.4, against which simplifications could be compared. The wind field was initialized as uniform easterly flow at 10 m/sec, and the lapse rate was constant at 6.5 °C per km. In Chapters 3 and 4, all runs are initialized at 6:00 a.m. local time and the plots of forecast zonal wind component versus time correspond to a height of 300 m and grid point 42. This point was chosen for the time evolution plots because it is just west of the base of the mountain, grid point 43 (in Fig. 2.4), and 300 m is the level at which the strongest low level winds are forecast for most runs, and the wind data is saved and plotted for every time step. The levels given in the vertical cross-sections are terrain following; thus, they are the atmospheric height above the topography at any given point. Fig. 3.7 is the forecast zonal wind component versus time for the control run. A 6-10 m/sec temporal oscillation, with a period of approximately an hour, can be seen in Fig. 3.7. This develops in all of the zonal wind versus time

plots. The cause of the temporal oscillation is not clear, but may be related to the secondary instability investigated by Peltier and Scinocca (1990; Fig. 4). They found the amplitude of the oscillation was as large as the time averaged response and the period was approximately 12 minutes for their nonlinear simulation. The temporal oscillation may also be a manifestation of dry convection as discussed later. The forecast zonal wind field for elapsed time of 18.0 hours (midnight local time) is given in Fig. 3.8, with easterly winds shown as solid contours and westerlies dashed. The wind field in this graph shows a flow reversal near 3 km, and grid point 44. This is similar to Durran (1986, Fig. 17) and appears to be caused by a vertical propagating wave with a very high amplitude.

Figs. 3.9 and 3.10 show cross-sections of the potential temperature field. At midnight local time (Fig. 3.9) there is a stable low level stratification with a temperature inversion in the lowest levels. The easterly wind component reaches a minimum shortly before noon as seen on Fig. 3.7. Fig 3.10 corresponds to noon and shows unstable stratification in the lowest 500 - 1000 m.

3.3.1 Vertical Mixing Coefficient

Runs were carried out to examine the sensitivity of the results when the parameterization of Eq. (2.6) was replaced by Eq. (2.12). During the day, the vertical mixing coefficient, as calculated from the full parameterization, is considerably larger than that given by the simplified version. Since at night the turbulent kinetic energy becomes small and the stability is large, the vertical mixing coefficient diminishes. Fig. 3.11 shows graphs of K_z versus time for a point 10 m above the surface, for each parameterization. Fig. 3.12 is similar, but at a height of 300 m.

With the simplified parameterization, the vertical mixing is too small during the day and too large at night. Fig. 3.13 displays the forecast zonal wind component versus time and Fig. 3.14 shows the forecast wind field at midnight, with the

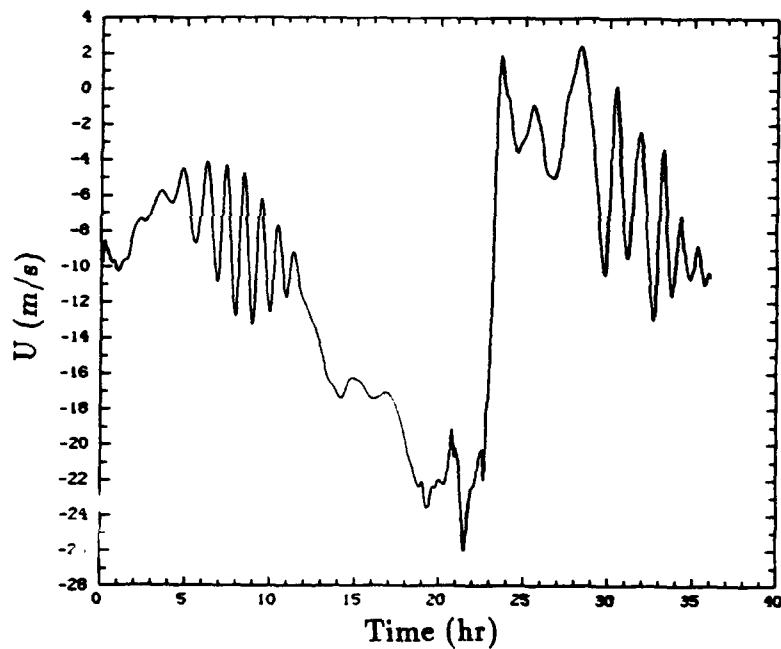


Figure 3.7. Forecast zonal wind component vs. time, for grid point 42 and height of 300 m, for the complete equations.

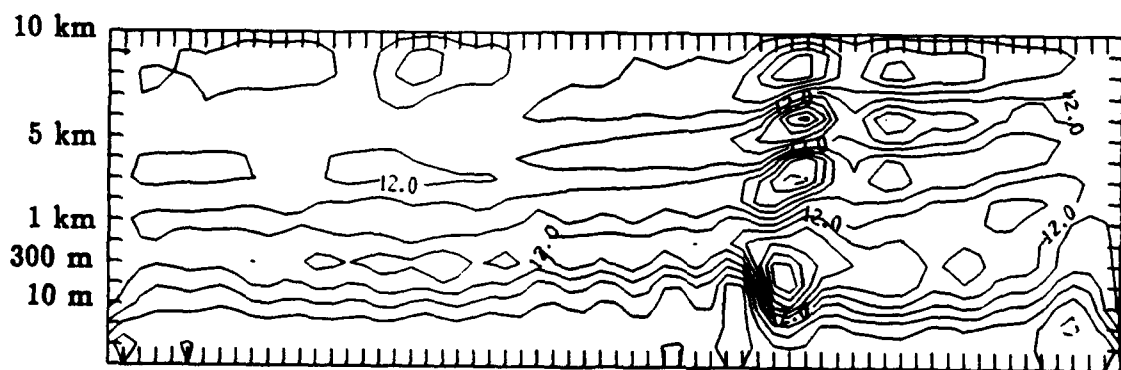


Figure 3.8. Vertical cross-section of forecast wind field at midnight local time. Contour interval is 3 m/sec.

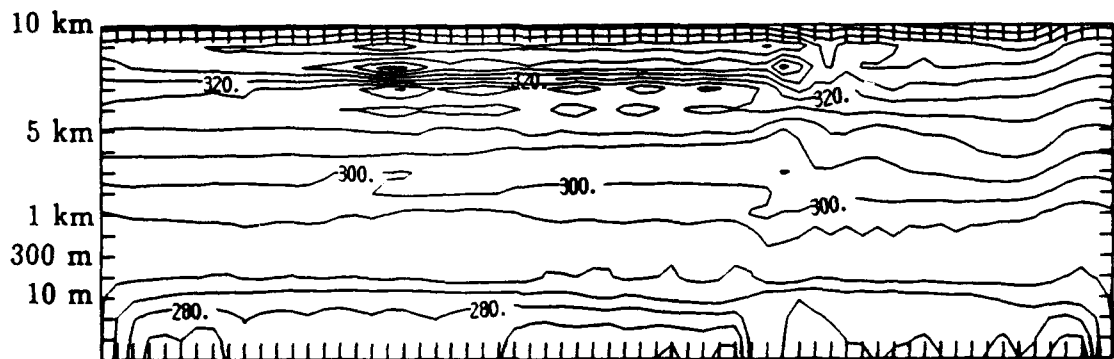


Figure 3.9. Vertical cross-section of potential temperature at midnight local time. Contour interval is $5^{\circ}K$.

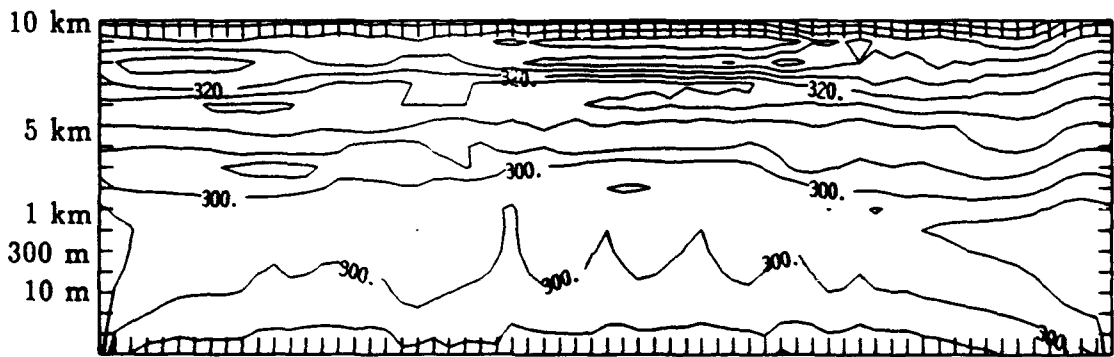


Figure 3.10. Vertical cross-section of potential temperature at noon local time on day two. Contour interval is $5^{\circ}K$.

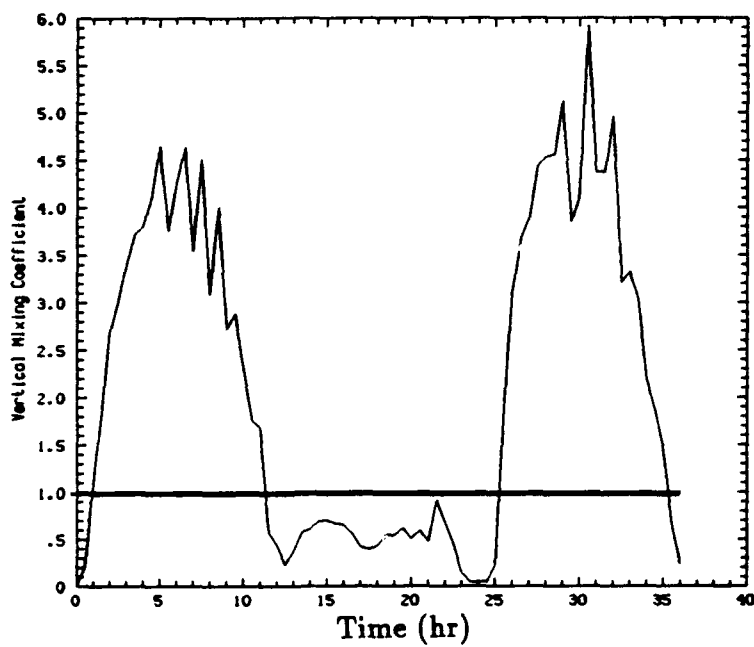


Figure 3.11. K_z vs. time for a height of 10 m. Thin line is derived from Eq. (2.6), bold line from Eq. (2.12).

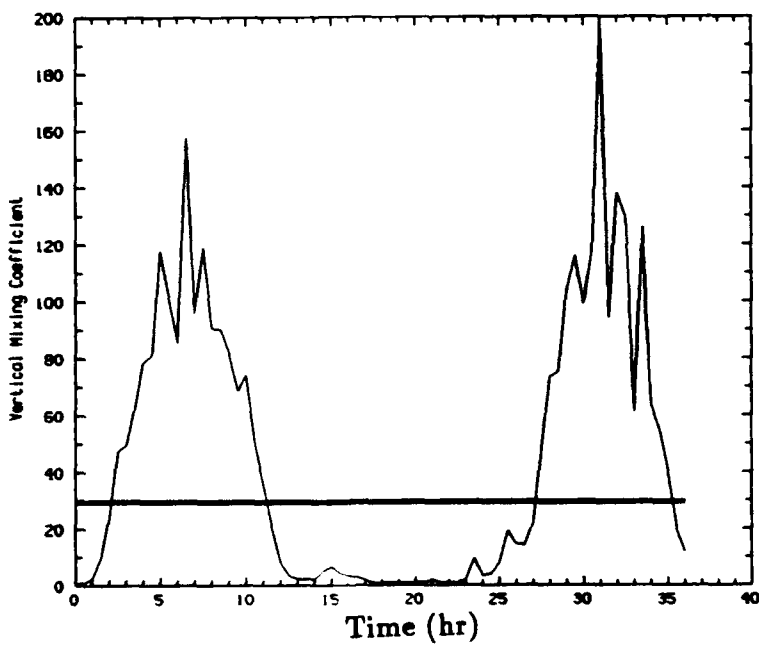


Figure 3.12. K_z vs. time for a height of 300 m. Thin line is derived from Eq. (2.6), bold line from Eq. (2.12).

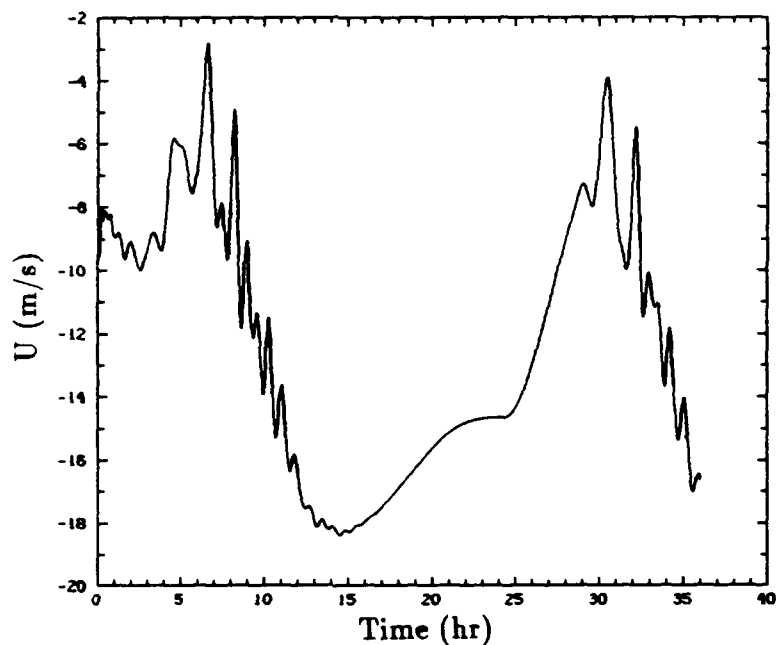


Figure 3.13. Forecast zonal wind component vs. time, for grid point 42 and height of 300 m with simplified K_z .

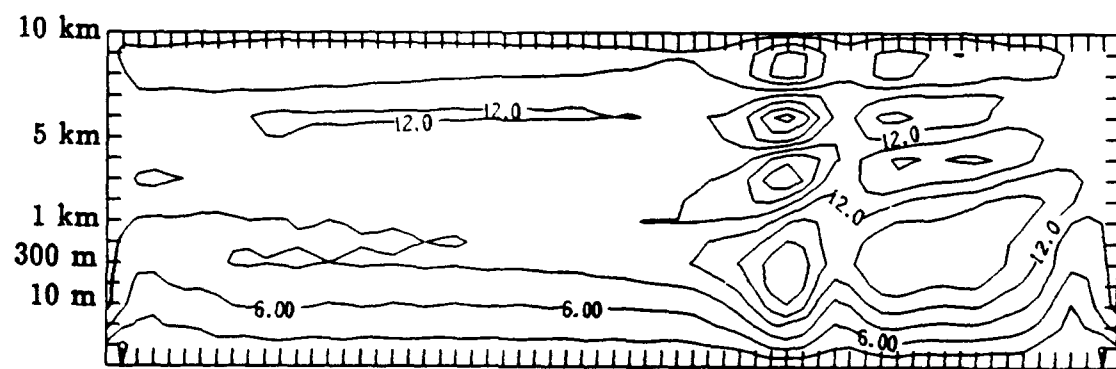


Figure 3.14. Vertical cross-section of forecast wind field with simplified K_z at midnight local time. Contour interval is 3 m/sec.

simplified parameterization for K_z . Figs. 3.15 and 3.16 correspond to Figs. 3.9 and 3.10 for the simplified vertical mixing coefficient run.

Comparing Fig. 3.7 to Fig. 3.13 shows the diurnal cycle is greatly weakened by simplifying the vertical mixing coefficient. In particular, Figs. 3.13 and 3.14 show much smaller nighttime windspeeds. The stronger nocturnal vertical mixing, produced by the simplified turbulence treatment, inhibits the formation of a nocturnal inversion, keeping neutral stratification in the low levels (see Fig. 3.15), and inhibits strong wind amplification. The complete parameterization used in Fig. 3.7 is essential to maintain the initial stable stratification; while the simplified vertical mixing coefficient allows regions of greater daytime instability to develop, as is shown in the potential temperature cross-sections. During the second day, strong short waves develop with the weaker vertical mixing (Fig. 3.16). It appears that these are a manifestation of dry convection. This speculation is supported by the fact that the waves are strongest in the region of deepest unstable stratification (near the center of the domain). They appear only when the stratification is unstable (compare Figs. 3.15 and 3.16), have higher amplitude in more unstable cases (compare Figs. 3.10 and 3.16), and are strongest for the shortest resolved horizontal scales. It is also possible that the mechanisms studied by Peltier and Scinocca (1990) contribute to the fluctuations. This high frequency oscillation may be strengthened in the two-dimensional case by the inability to disperse gradients in the North-South direction. The effects of varying the stability will be looked at in more detail in Chapter 4.

3.3.2 Radiation

In one series of runs, the radiation flux terms were removed, eliminating the diurnal cycle from the results. Fig. 3.17 shows that temporal oscillations are apparent, even without radiation terms, supporting the hypothesis that these oscillations are

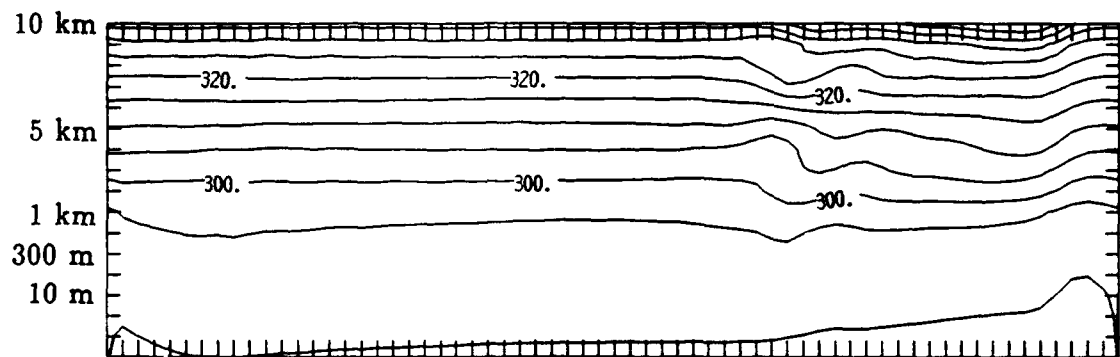


Figure 3.15. Vertical cross-section of potential temperature with simplified K_z at midnight local time. Contour interval is $5^{\circ}K$.

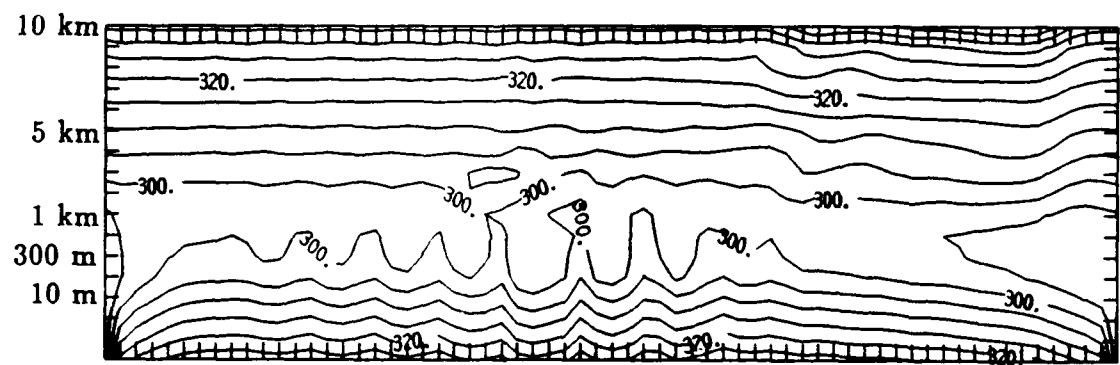


Figure 3.16. Vertical cross-section of potential temperature with simplified K_z at noon local time on day two . Contour interval is $5^{\circ}K$.

related to the phenomena investigated by Scinocca and Clark (1989, 1990), since their model did not have a diurnal cycle.

The forecast wind field corresponding to Fig. 3.8, without radiation terms (Fig. 3.18), shows the maximum easterly wind component is the same strength as that found in Fig. 3.8, but is located further upstream. The low level maximum is at grid point 53 on Fig. 2.4, which is on the downslope of the higher ridge. Potential temperature cross-sections are shown in Figs. 3.19 and 3.20. There is little difference between the potential temperature graphs, each showing a deep neutral layer which extends through the lowest kilometer of the atmosphere. Without radiational terms, there is no change to the forcing between the times, thus this similarity is expected.

The peak windspeeds for all of these experiments have been found to be a nocturnal occurrence, beginning to decrease after 22 hours. Thus in the next section, the runs will be shortened to 24 hours.

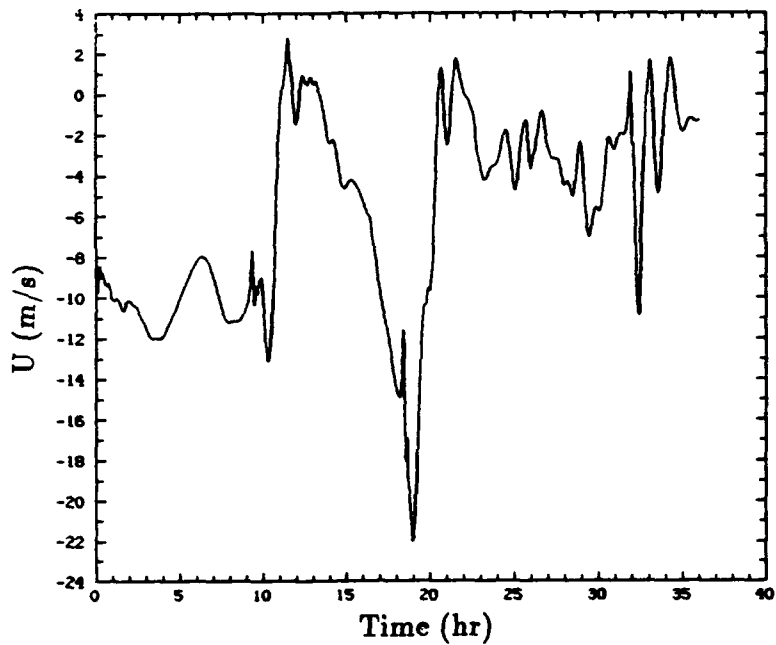


Figure 3.17. Forecast zonal wind component vs. time, for grid point 42 and height of 300 m, without radiation terms.

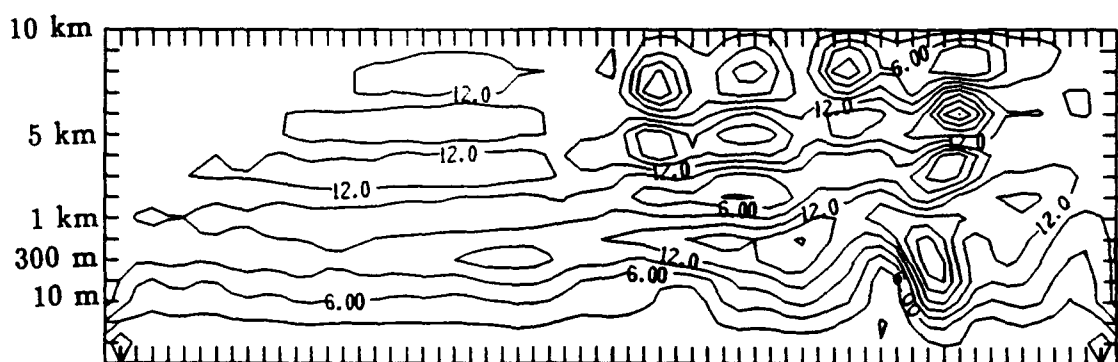


Figure 3.18. Vertical cross-section of forecast wind field without radiation terms at midnight local time. Contour interval is 3 m/sec.

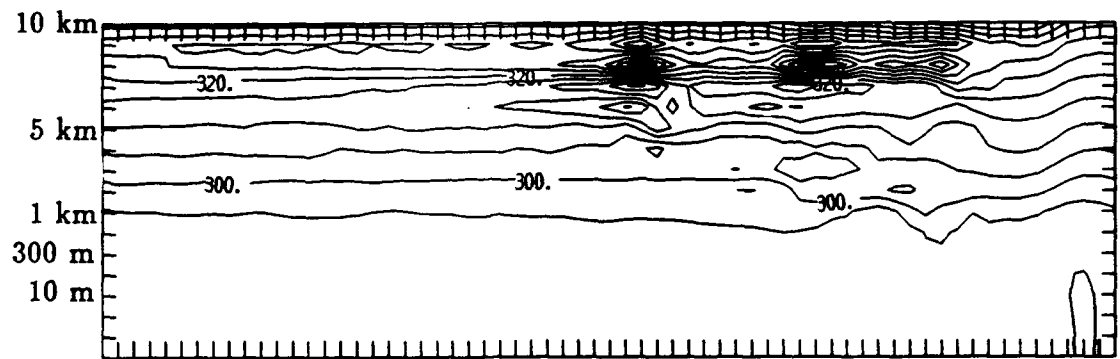


Figure 3.19. Vertical cross-section of potential temperature without radiation terms at midnight local time. Contour interval is $5^{\circ}K$.

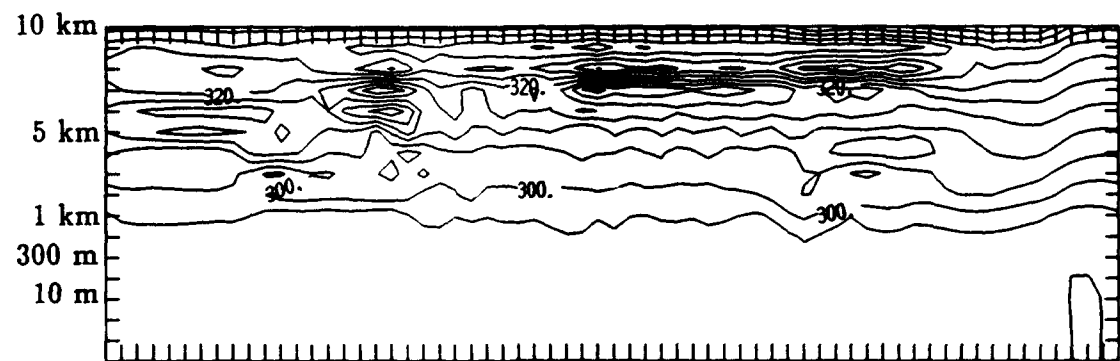


Figure 3.20. Vertical cross-section of potential temperature without radiation terms at noon local time on day two. Contour interval is $5^{\circ}K$.

CHAPTER 4

PHYSICAL EXPERIMENTS

Even in regions prone to downslope windstorms, strong events are not an everyday occurrence. Julian and Julian (1969) found an average of just over one severe windstorm per year in the Boulder area. Therefore, certain atmospheric parameters must be instrumental in the forcing required for strong wind amplification. One of the tasks here is to help isolate these factors.

In this chapter, the topographical profile given in Fig. 2.4 will again be used and the runs remain two-dimensional. The model is initialized at 6:00 a.m., which roughly corresponds to sunrise.

4.1 Vertical Wind Profiles

An essential condition for downslope winds is that the low level windflow must be nearly perpendicular to the mountain range. However, this requirement can be met while varying the vertical structure of the windfield. Three types of vertical wind profiles were tested: easterly - constant with height (the same as the control run in the previous section), easterly - linearly increasing to 700 mb then constant above, and easterly flow at low levels, decreasing to zero slightly above mountaintop level, then westerly aloft.

In all of these profiles, the winds below 10 m decrease logarithmically to zero at the surface. Figs. 4.1-4.3 show the initial wind fields as outlined above, for a point west of the mountain. The winds are initialized on pressure surfaces.

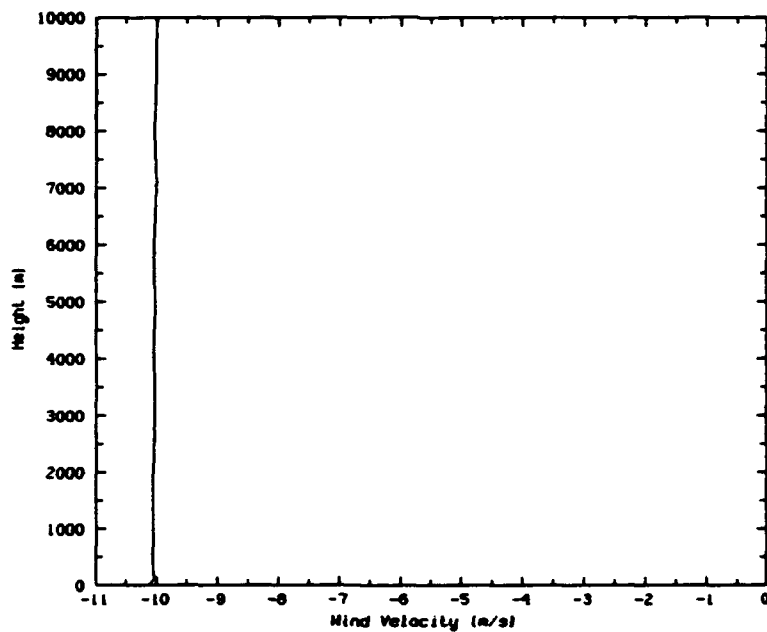


Figure 4.1. Initial wind profile for constant wind with height.

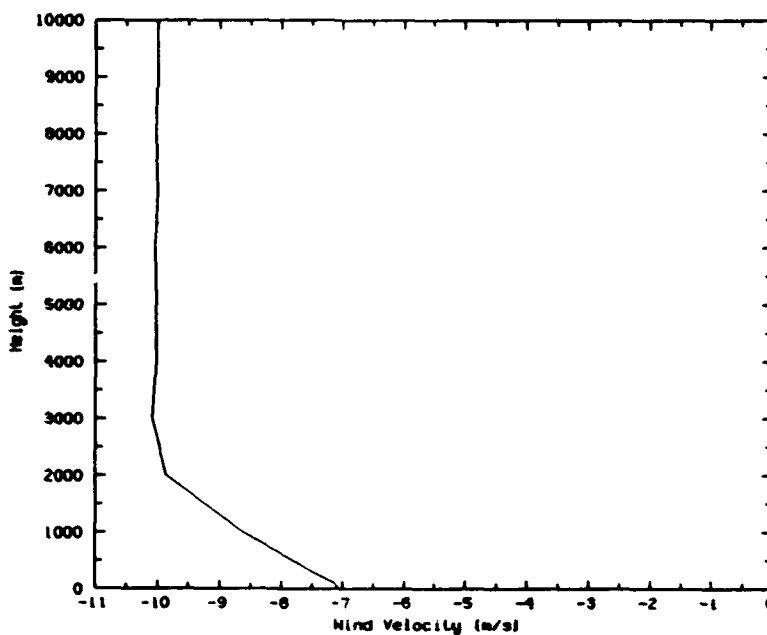


Figure 4.2. Initial wind profile for linearly increasing winds.

The mountaintop elevation is approximately 1 km above the plain; thus the initial surface winds correspond to those shown on Figs. 4.1-4.3 at 1 km. The resulting forecast zonal wind component versus time plots, for grid point 42 from Fig. 2.4 at a height of 300 m, are shown in Figs. 4.4-4.6. The zonal wind evolution for the linearly increasing wind forecast (Fig. 4.5) is not representative of the strongest wind field. The wind maximum in this case is very narrow and is centered between grid points 43 and 44. Thus grid point 42 is downstream of the maximum at all but near 19 hours. At this time the maximum is wide enough to include grid point 42 and it appears as a spike in Fig. 4.5. The third case, with the winds reversing with height, develops the strongest amplification, consistent with the findings of other investigators.

Figs. 4.7-4.8 show the forecast vertical cross-sections of the zonal component of the wind fields for profiles shown in Figs. 4.2-4.3, respectively. Fig. 3.8 is the corresponding cross-section for the profile shown in Fig. 4.1. Easterly winds are depicted as solid contours and westerlies are dashed. The vertical cross-sections of the wind for the constant and linearly increasing forecast wind fields are very similar. The horizontal extent of the maximum is larger in the reversing wind case, as well as being slightly stronger. Clark and Peltier (1984) concluded that not only could a wind reversal with height significantly increase the strength of surface drag, but the level at which the wind reversal occurred was also critical.

4.2 Stability

In the above comparison of vertical wind profiles, the lapse rate was initialized at 6.5 °C per km throughout the troposphere. In this series of experiments, inversions were inserted at different levels, using the initial wind profile illustrated in Fig. 4.3. Results will be compared for three cases: constant stability in the troposphere (lapse rate = 6.5 °C per km), a surface based inversion, and an inversion based

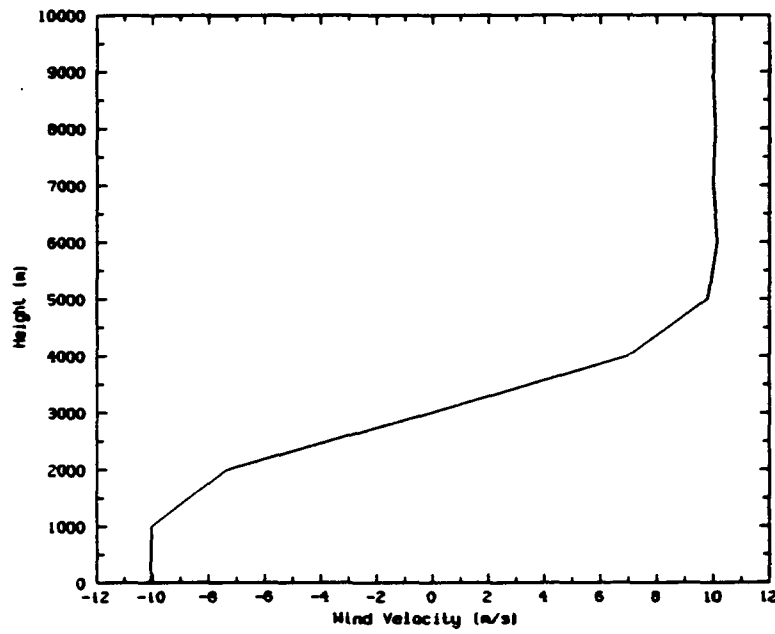


Figure 4.3. Initial wind profile for a reversing wind field.

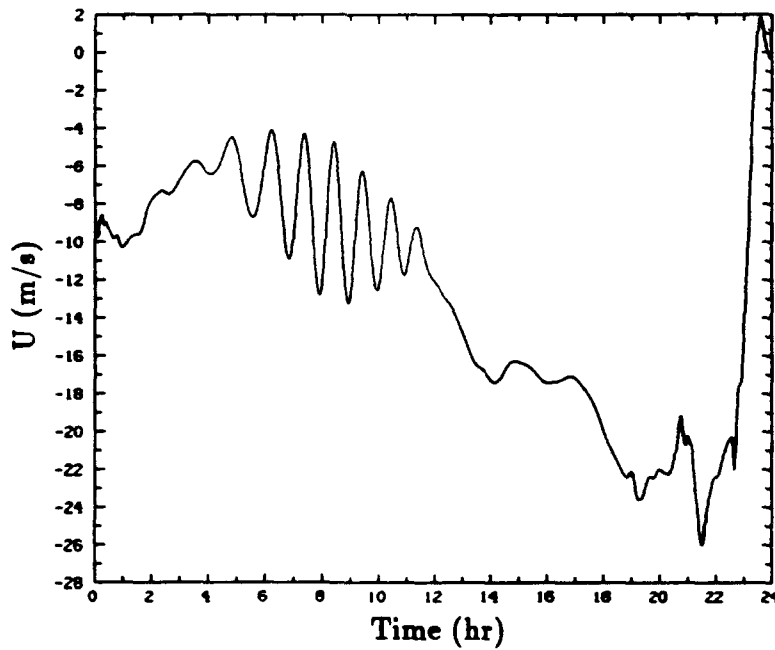


Figure 4.4. Forecast zonal wind component vs. time, for grid point 42 at 300 m, using profile shown in Fig. 4.1. Same as Fig. 3.7, but truncated after 24 hours.

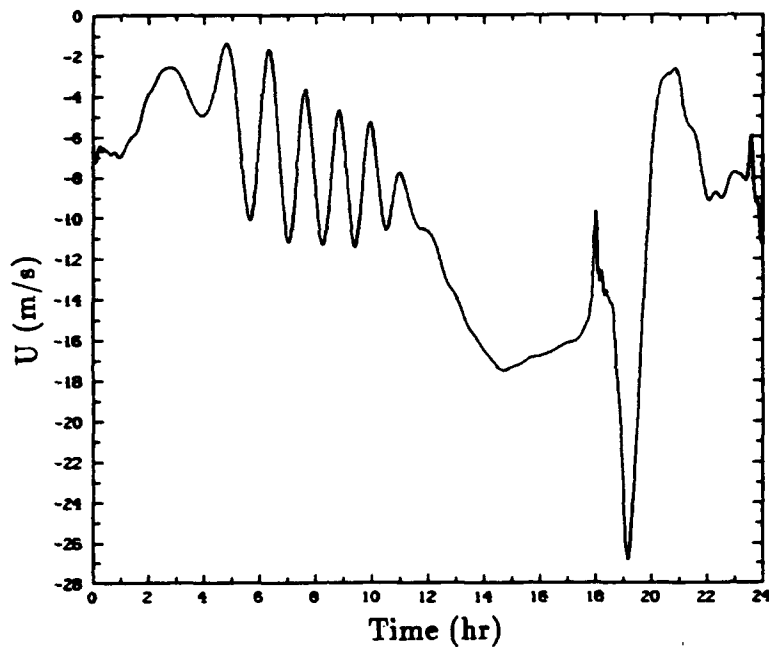


Figure 4.5. Forecast zonal wind component vs. time, for grid point 42 at 300 m, using profile shown in Fig. 4.2.

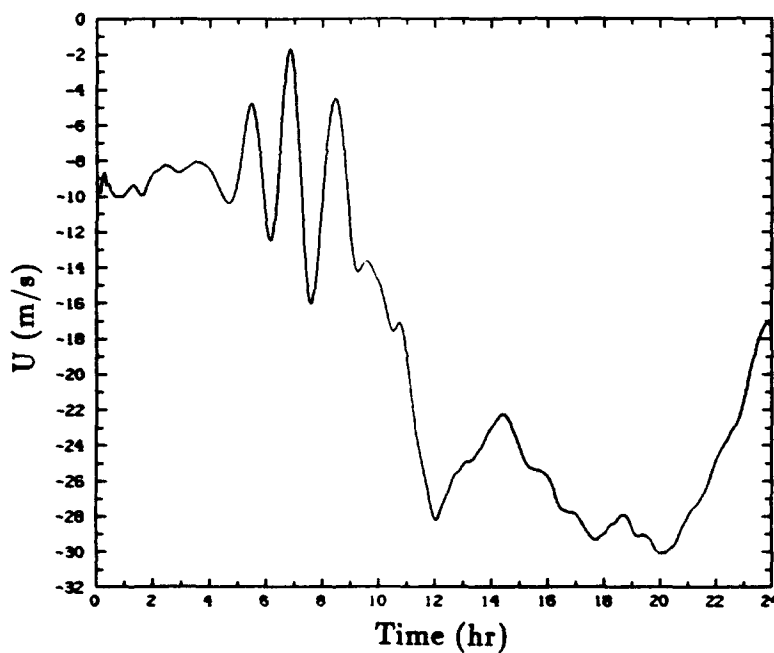


Figure 4.6. Forecast zonal wind component vs. time, for grid point 42 at 300 m, using profile shown in Fig. 4.3.

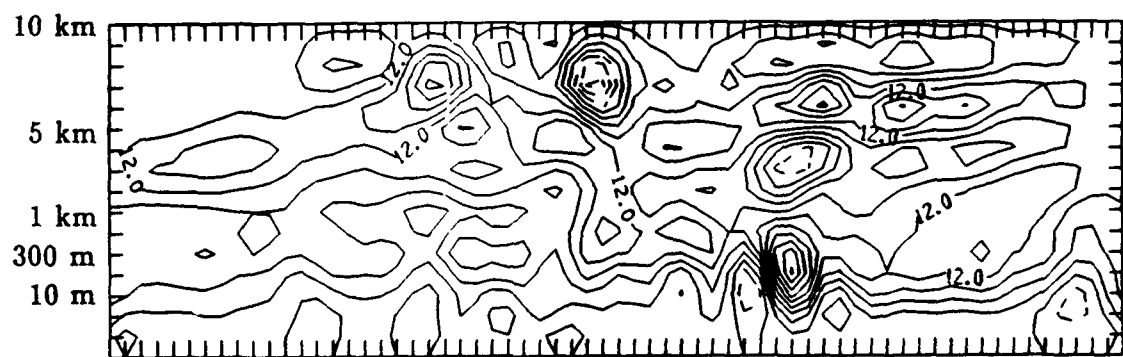


Figure 4.7. Vertical cross-section of forecast wind field for initial profile shown in Fig. 4.2. at midnight local time. Contour interval is 3 m/sec.

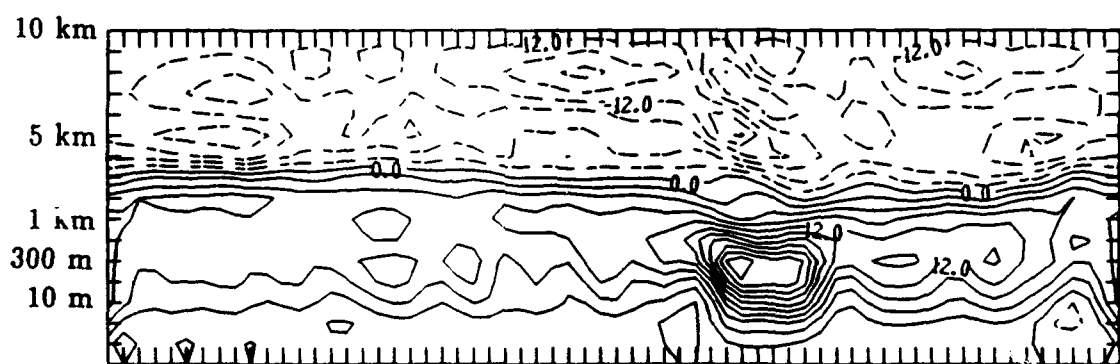


Figure 4.8. Vertical cross-section of forecast wind field for initial profile shown in Fig. 4.3. at midnight local time. Contour interval is 3 m/sec.

near mountaintop, with nearly neutral conditions below. The initial temperature profiles, for a point west of the mountain are shown in Figs. 4.9-4.11.

The forecast zonal wind component time evolution plots are given in Figs. 4.12-4.13 and Figs. 4.14-4.15 show the vertical cross-sections of the forecast zonal wind field at midnight local time for the two inversion cases. Neither of the runs with inversions developed as strong winds near the base of the mountain as did the constant stability run. In the run initialized with a surface inversion, the vertical cross-section (Fig. 4.14) shows a double maxima, separated by a low-level region of flow reversal. This region of flow reversal occurs between grid points 47 and 49 and is located in the valley between the two ridges. The stronger of the two maxima is the one further upstream, near grid point 51. The wind maximum begins to develop near grid point 55 and propagates downstream in the mountaintop inversion case. In this run, the wind appears to continue to accelerate even between grid points 48 and 46, where it is traveling up the smaller peak. This is a characteristic of the

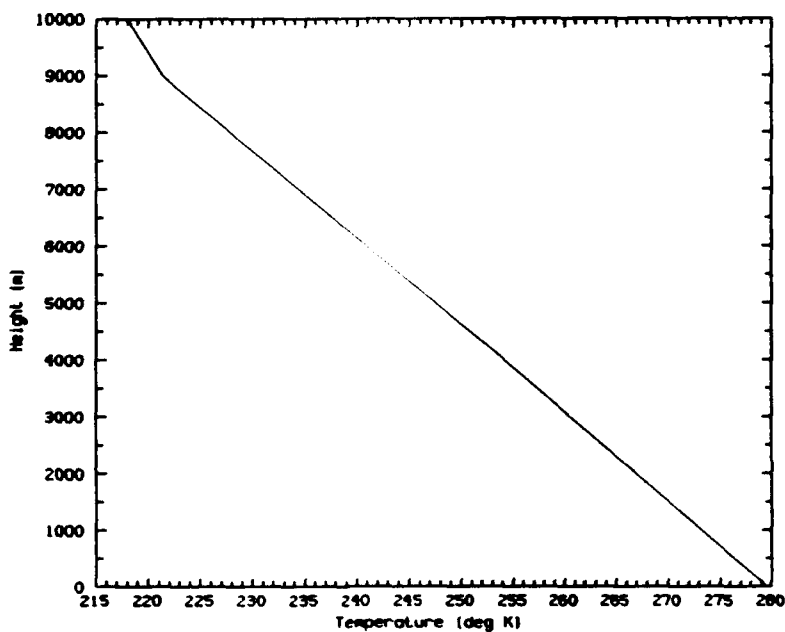


Figure 4.9. Initial temperature profile for constant stability case.

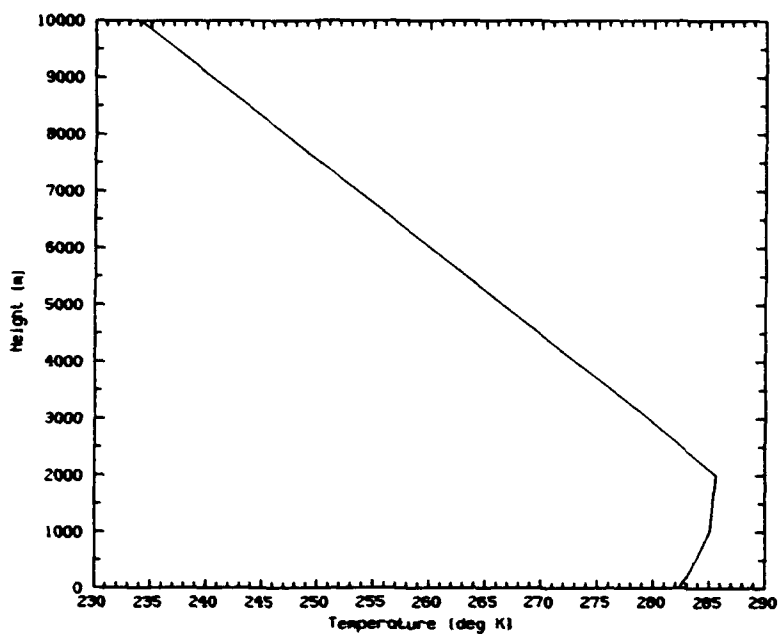


Figure 4.10. Initial temperature profile for a surface based inversion.

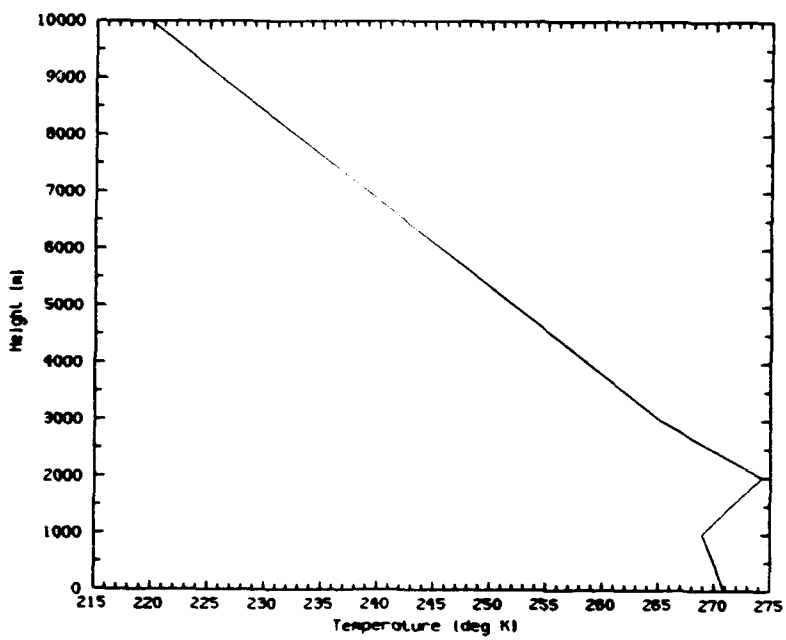


Figure 4.11. Initial temperature profile for an inversion based near mountaintop.

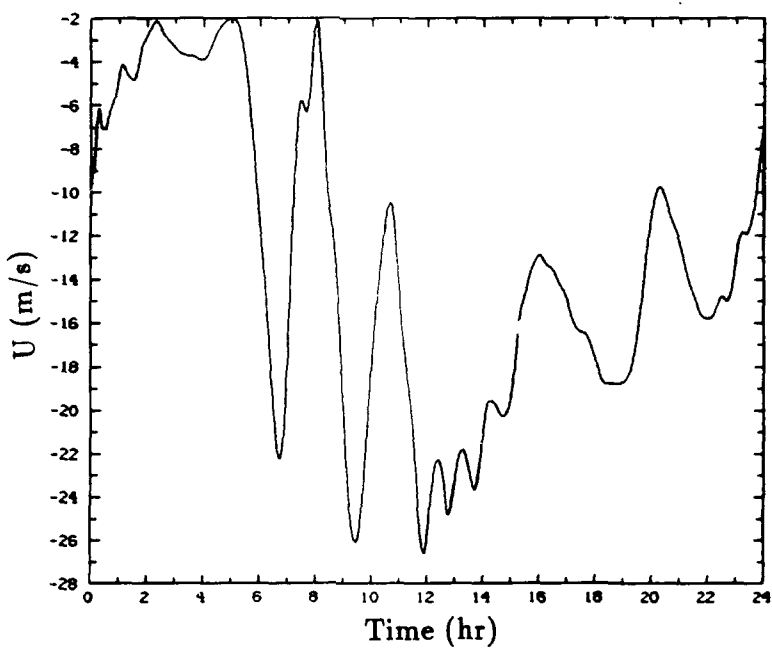


Figure 4.12. Forecast zonal wind component vs. time plot, for grid point 42 at 300 m, using profile given in Fig. 4.10.

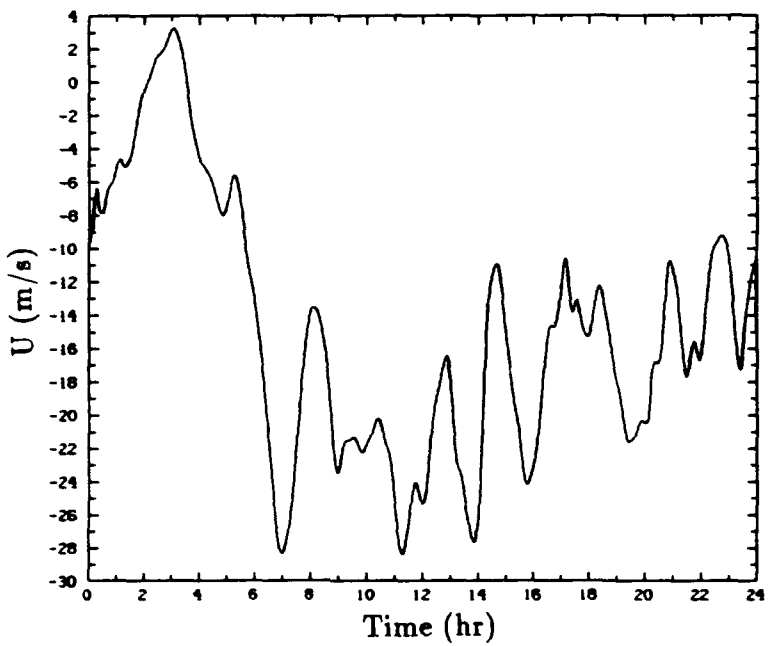


Figure 4.13. Forecast zonal wind component vs. time plot, for grid point 42 at 300 m, using profile given in Fig. 4.11.

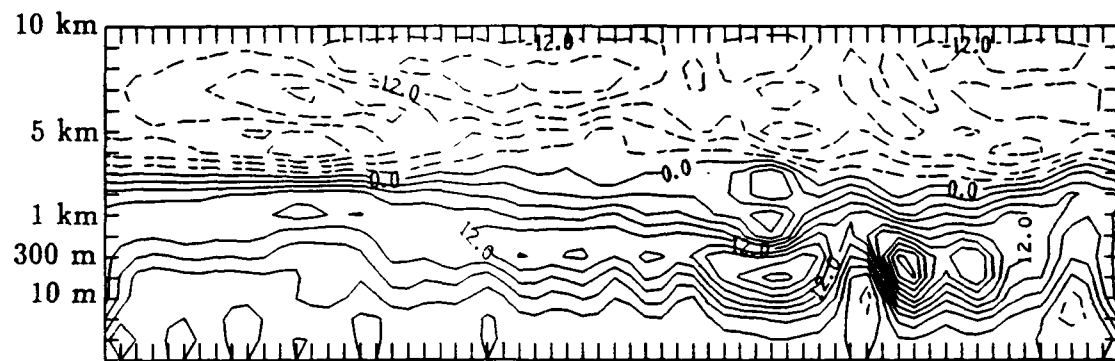


Figure 4.14. Vertical cross-section of forecast wind field for initial profile shown in Fig. 4.10. at midnight local time. Contour interval is 3 m/sec.

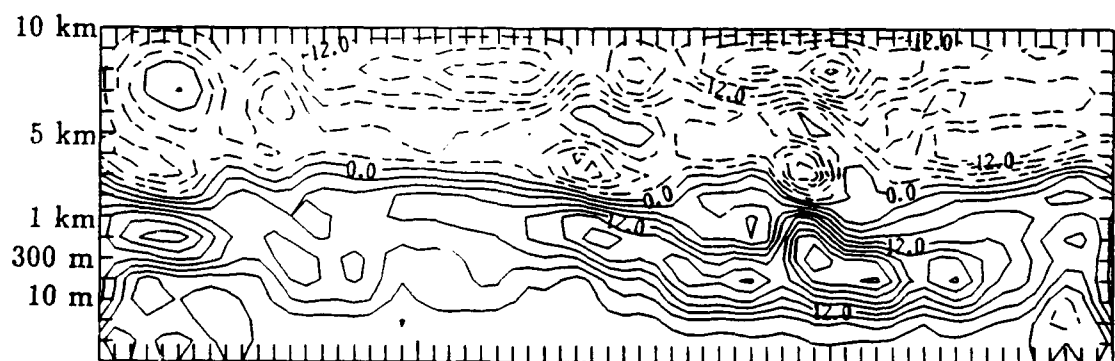


Figure 4.15. Vertical cross-section of forecast wind field for initial profile shown in Fig. 4.11. at midnight local time. Contour interval is 3 m/sec.

hydraulic jump theory (Durran, 1990).

The dependence that other investigators have found between the wind speed and an elevated inversion is not evident here. However the forecast wind field does show a sensitivity to the initial stability profile which appears to be consistent with the results of Klemp and Lilly (1975) in that the position of the maximum surface velocity is dependent on the stability profile.

4.3 Dynamical Interpretation

The components of the horizontal momentum equations were evaluated and compared to determine the primary forcing mechanism when strong downslope winds were forecast. Combining the momentum equations, (2.1) - (2.2), in vector form:

$$\frac{\partial \bar{V}}{\partial t} + (\bar{V} \cdot \nabla) \bar{V} + f K \times \bar{V} = -\frac{1}{\rho_s} \nabla P' - \frac{\rho'}{\rho_s} g \nabla Z_T + \text{Friction.} \quad (4.1)$$

The friction term was neglected for this quantitative analysis. Using the vector identity:

$$(\bar{V} \cdot \nabla) \bar{V} = \nabla \left(\frac{\bar{V} \cdot \bar{V}}{2} \right) + K \times \bar{V} \zeta, \quad (4.2)$$

where ζ is relative vorticity and rearranging terms, yields:

$$\frac{\partial \bar{V}}{\partial t} = -(f + \zeta) K \times \bar{V} - \frac{1}{\rho_s} \nabla P' - \nabla \left(\frac{\bar{V} \cdot \bar{V}}{2} \right) - \frac{\rho'}{\rho_s} g \nabla Z_T. \quad (4.3)$$

Thus examining only the east-west components:

$$\frac{\partial u}{\partial t} = -(f + \zeta) v - \left[\frac{1}{\rho_s} \frac{\partial P'}{\partial x} + \frac{1}{2} \frac{\partial |\bar{V}|^2}{\partial x} + \frac{\rho' g}{\rho_s} \left(\frac{\partial Z_T}{\partial x} \right) \right]. \quad (4.4)$$

The local acceleration term is balanced by the Coriolis, pressure gradient, Bernoulli, and differential height terms. The differential height term, which may be significant in regions of undulating terrain, should however be small to the west of the mountains. Figs. 4.16-4.21 are graphical analyses of these five terms and the residual, after 18 hours, for the run with a reversing wind profile and the stability profile

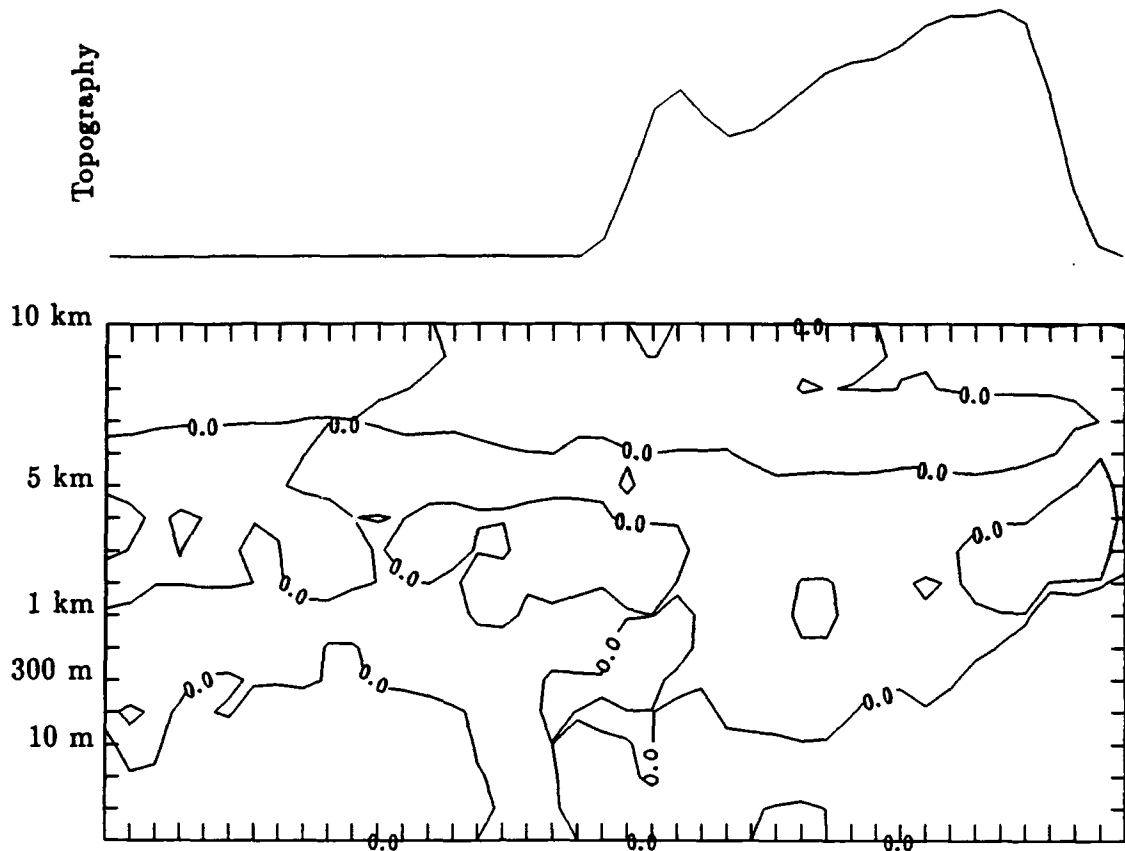


Figure 4.16. Coriolis contribution of Eq. (4.4). Contour interval is .005 m/sec².

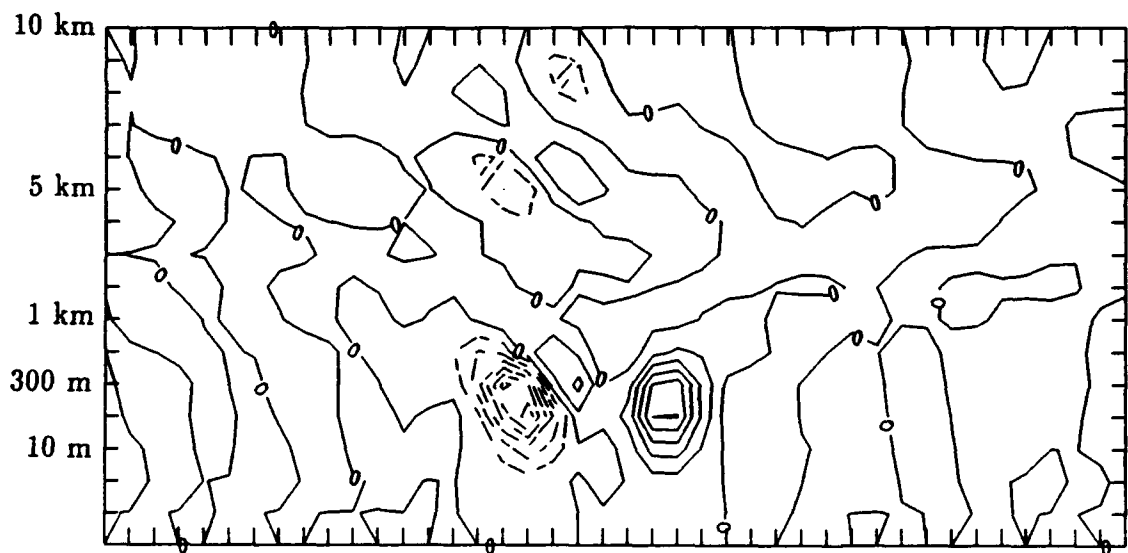


Figure 4.17. Bernoulli contribution of Eq. (4.4). Contour interval is .005 m/sec².

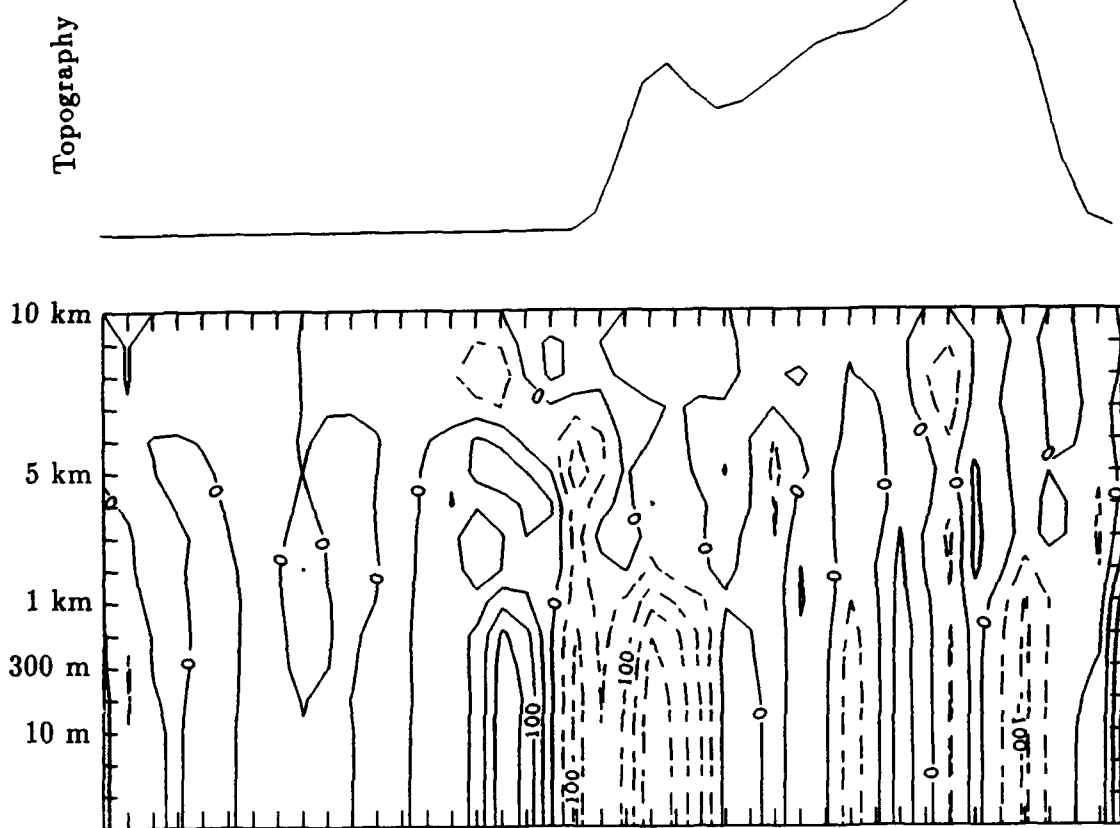


Figure 4.18. Pressure gradient contribution of Eq. (4.4). Contour interval is .005 m/sec^2 .

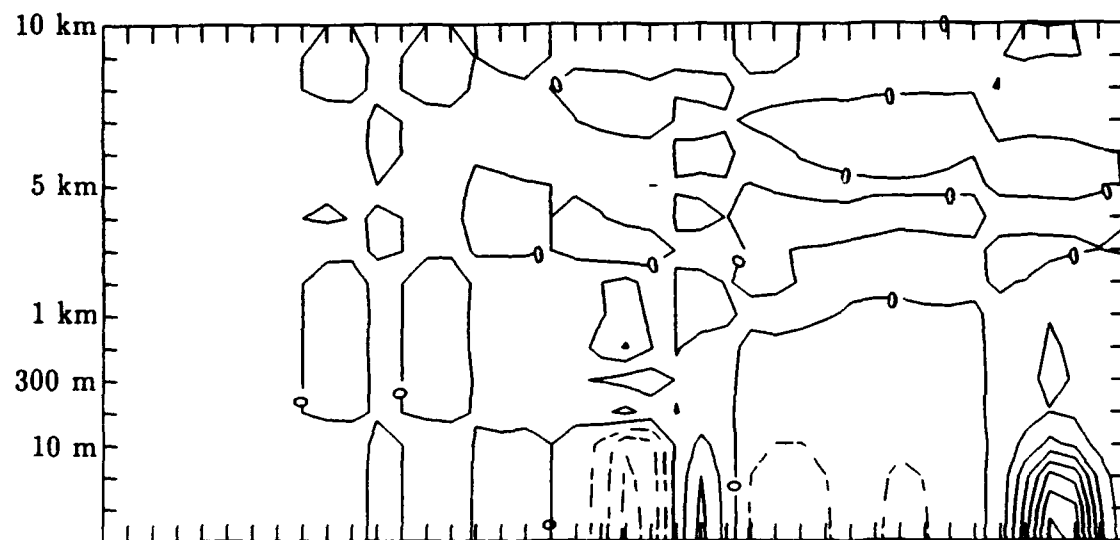


Figure 4.19. Terrain contribution of Eq. (4.4). Contour interval is .005 m/sec^2 .

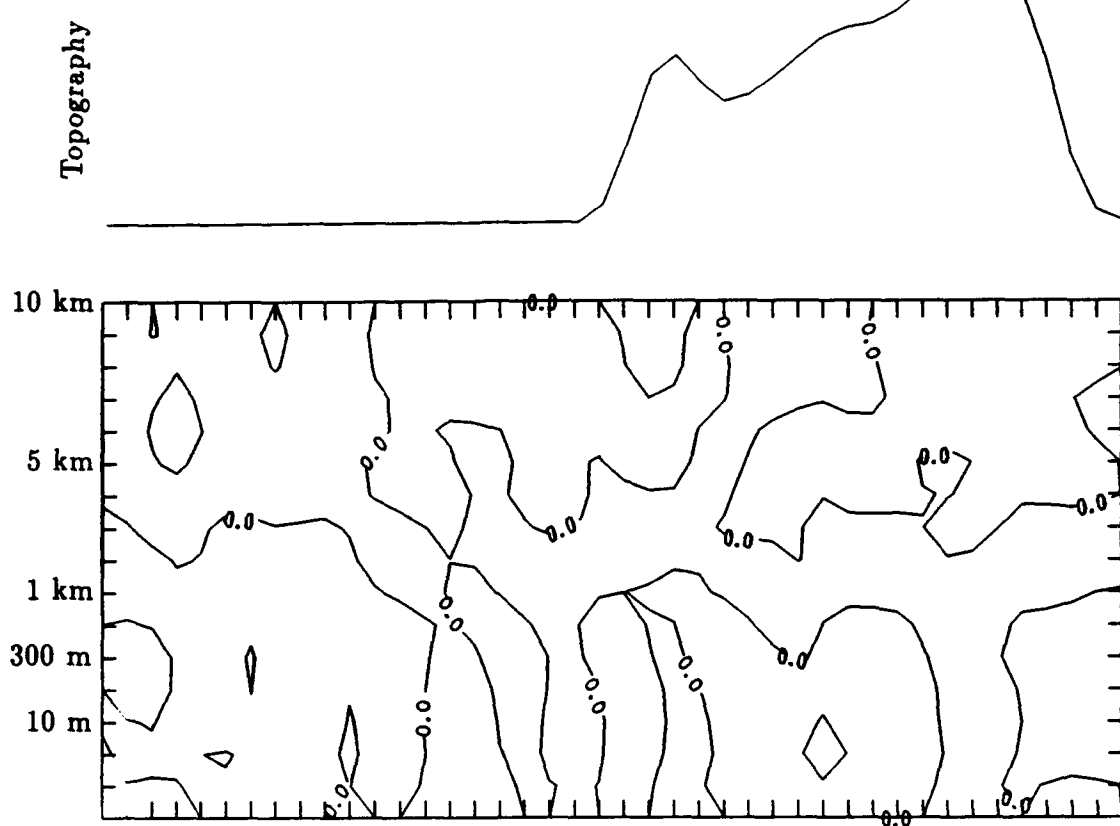


Figure 4.20. Local acceleration term of Eq. (4.4). Contour interval is .005 m/sec².

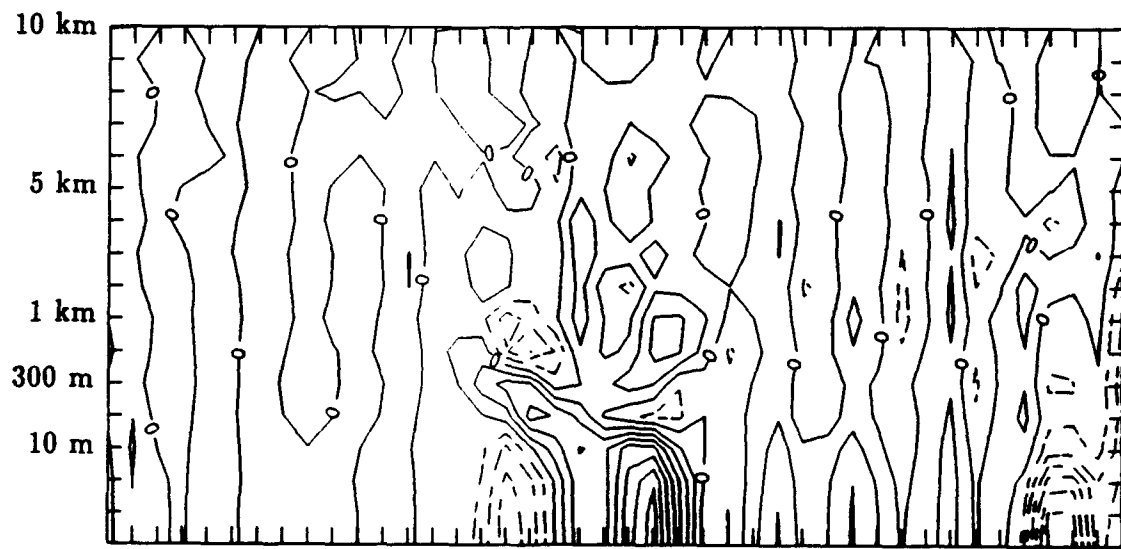


Figure 4.21. Residual for Eq. (4.4). Contour interval is .005 m/sec².

in Fig. 4.9. The contour interval was held constant at $.005 \text{ m/sec}^2$. Grid points 1-22 are omitted on the figures in this section to focus on the region immediately surrounding the higher terrain. On the top of each page is an outline of this modified terrain for comparison.

Analysis of these figures shows that the essential balance includes the Bernoulli, pressure gradient and differential terrain terms. The Bernoulli term acts counter to the pressure gradient and terrain following terms in the region of interest and the Coriolis term is negligible for this forcing and scale of domain. The local acceleration term is an order of magnitude smaller than the Bernoulli, pressure gradient, and terrain following terms. The residual field was calculated by subtracting the terms on the right hand side of the equation from the local acceleration term, and shows the effects due to mixing and diffusion. The mixing and diffusion terms were not calculated for this comparison due to their implicit nature. Table 4.1 shows the minimum and maximum values for each term.

4.4 Examination of Downstream Wind Profile

Lilly and Klemp (1975) noted that observations near Boulder, CO have shown that the region of strong winds has a maximum in Boulder, then diminishes rapidly to the east. Arakawa (1969) studied the Hokkaido, Japan region, and cited 4 km from the base of the mountains as the region where most damage from downslope winds is confined. National Weather Service observations near the Wasatch Moun-

Table 4.1. Quantitative values for components of the momentum equation.

Momentum equation term	Minimum value	Maximum value
Coriolis	$-.001 \text{ m/sec}^2$	$.001 \text{ m/sec}^2$
Bernoulli	$-.033 \text{ m/sec}^2$	$.024 \text{ m/sec}^2$
Pressure gradient	$-.024 \text{ m/sec}^2$	$.018 \text{ m/sec}^2$
Terrain	$-.015 \text{ m/sec}^2$	$.036 \text{ m/sec}^2$
Local acceleration	$-.003 \text{ m/sec}^2$	$.002 \text{ m/sec}^2$
Residual of Eq. 4.4	$-.032 \text{ m/sec}^2$	$.036 \text{ m/sec}^2$

tains during the strong wind event that occurred on 15 December 1988 recorded light winds at the Salt Lake City airport of about 10 mph, while winds in Centerville, UT, a distance of less than 25 km away, were estimated at 110 mph.

Since observations are taken at low levels, the winds at a height of 10 m were graphed to study the horizontal extent of the strong wind amplification for the reversing wind profile with constant stability run (Figs. 4.3 and 4.9). Fig. 4.22 is a plot of the forecast windspeed divided by the initial windspeed versus grid point at a local midnight forecast time. The strongest amplification occurs near the base of the mountain (grid point 44) and in less than 4 grid points downstream from the base of the mountain, approximately 23 km, the amplification decreases to less than the initial windspeed.

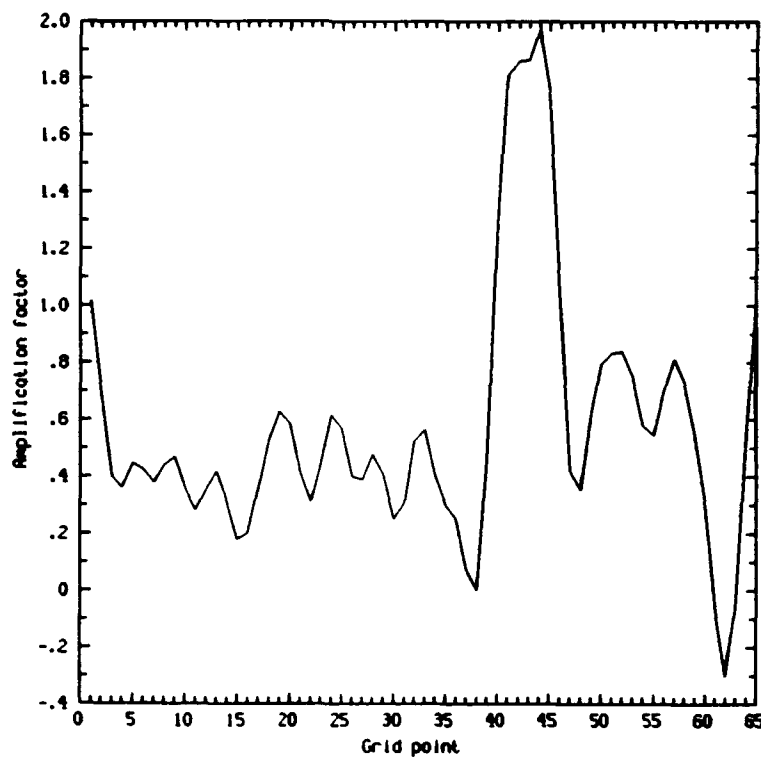


Figure 4.22. Wind amplification vs. grid point at a height of 10 m.

CHAPTER 5

EXPERIMENTS IN THREE DIMENSIONS

In order to run the model in two dimensions, several simplifications were required: diffusion was eliminated in the north-south direction, initial temperatures were maintained on the north and south boundaries, and topography was constant in the north-south direction. A three-dimensional simulation was made to evaluate these effects. The domain was chosen such that the terrain used in the two-dimensional runs would be near the center, and thus removed from boundary effects, for better comparison between the cases.

5.1 Domain and Initialization

East-west cross-sections of topography from northern Utah were processed according to procedures in section 2.5, with interpolation to 33 grid points, for a grid size of 11.5 km. This was done for 17 terrain slices, with north-south grid spacing of 14.7 km. The resulting terrain is depicted in Fig. 5.1. The X-Z cross-section at J=10 corresponds to the profile that was used for the two-dimensional runs, except the terrain at the base of the mountain was not smoothed.

The model simulation was initialized with a reversing wind profile (Fig. 4.3) and constant lapse rate (Fig. 4.9).

5.2 Results

The forecast u wind component versus time plot for a point corresponding to I=20 and J=10 on Fig 5.1, at a height of 300 m, is shown in Fig 5.2. This point



Figure 5.1. Terrain for three-dimensional run. Contour interval is 100 m.

chosen to correspond to that in Fig 4.6. The maximum windspeed in the three-dimensional run occurs about 5 hours later and is about 20 m/sec stronger than in the two-dimensional run. The high frequency oscillations are weaker in the three-dimensional run than in Fig. 4.6. This may be due to more realistic wave dispersion in the three-dimensional case. The horizontal maps of the forecast wind fields, at heights of 10 and 300 m, and time of 18.0 hours, are shown in Figs. 5.3 and 5.4. In Fig. 5.5, the vector wind field, corresponding to Fig. 5.4, is shown superimposed on the topography contours. It is evident that the strongest winds are located near the lee of the steepest topography, as would be expected.

Vertical east-west cross-sections of the forecast wind field at 18.0 hours are shown for two positions. Figs. 5.6 and 5.7 display the terrain profile and forecast wind field for $J=7$, which is the slice where the strongest winds occur. Figs. 5.8 and 5.9 show the same graphs at $J=10$, corresponding to the terrain used in the two-dimensional cases; thus, we can compare Figs. 5.9 and 4.8. The magnitude and patterns of the

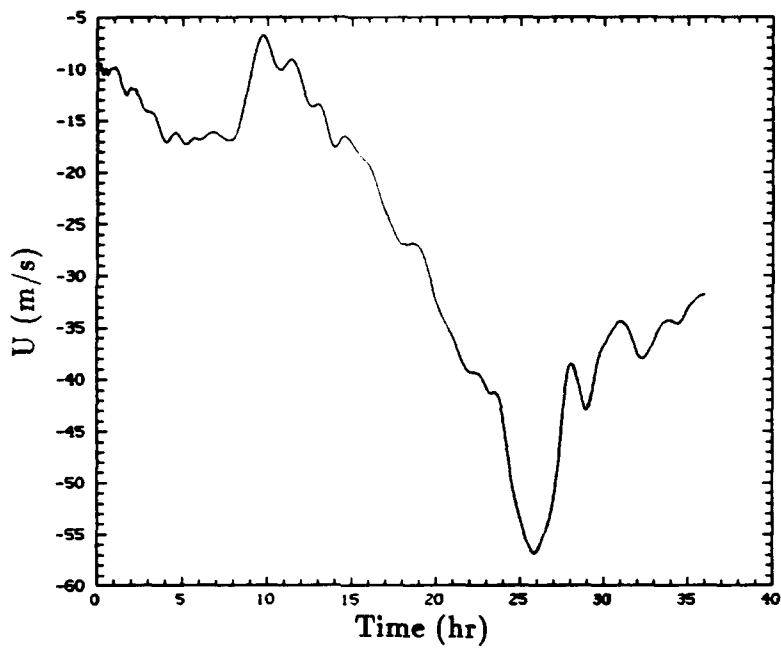


Figure 5.2. Forecast u wind component vs. time plot for point $I=20$, $J=10$, at a height of 300 m.

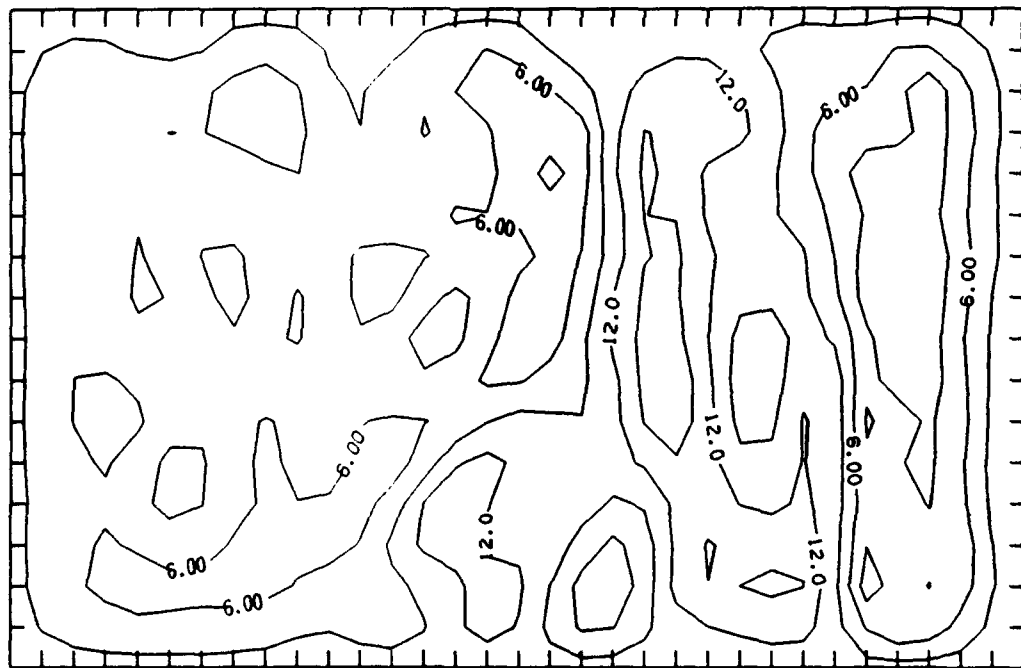


Figure 5.3. Horizontal map of forecast winds at a height of 10 m. Contour interval is 3 m/sec.

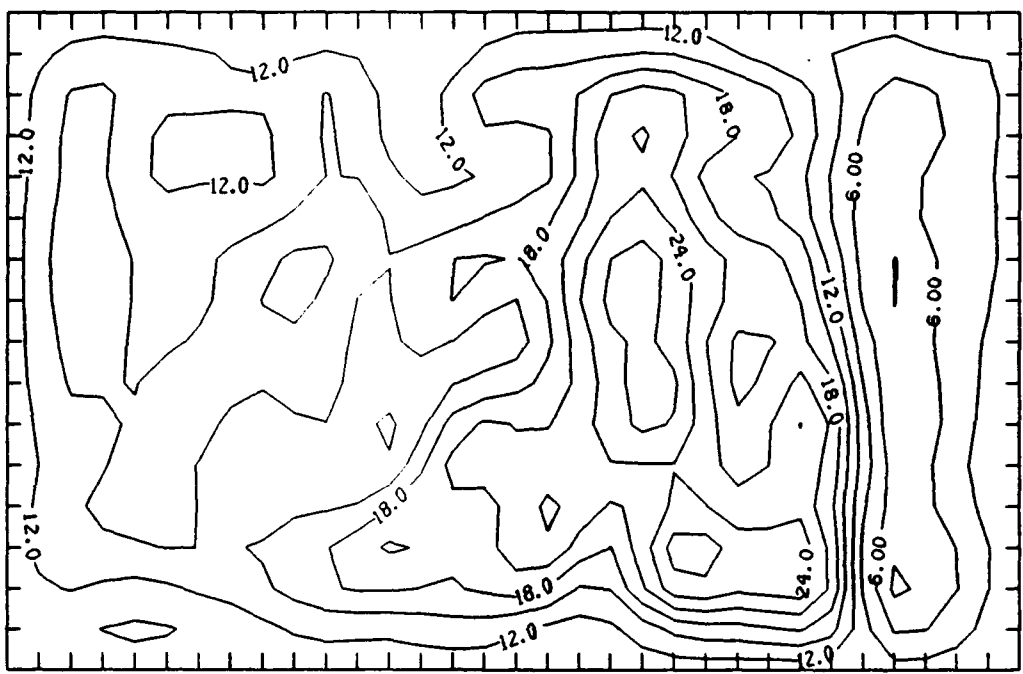


Figure 5.4. Horizontal map of forecast wind field at a height of 300 m. Contour interval is 3 m/sec.

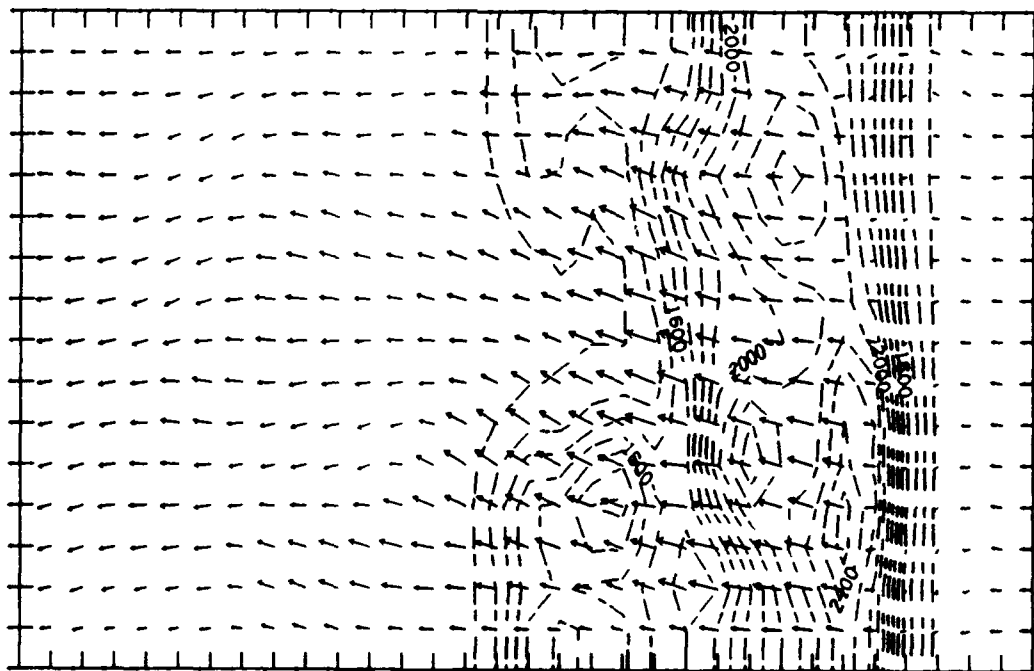


Figure 5.5. Horizontal map of forecast vector winds at a height of 300 m. Contour interval for topography is 100 m.

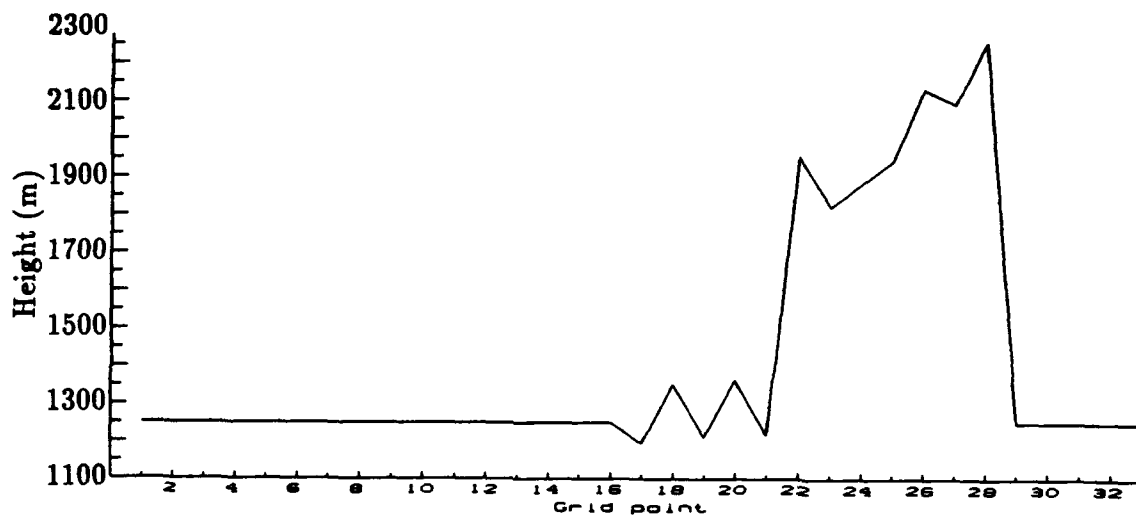


Figure 5.6. Terrain profile at $J=7$.

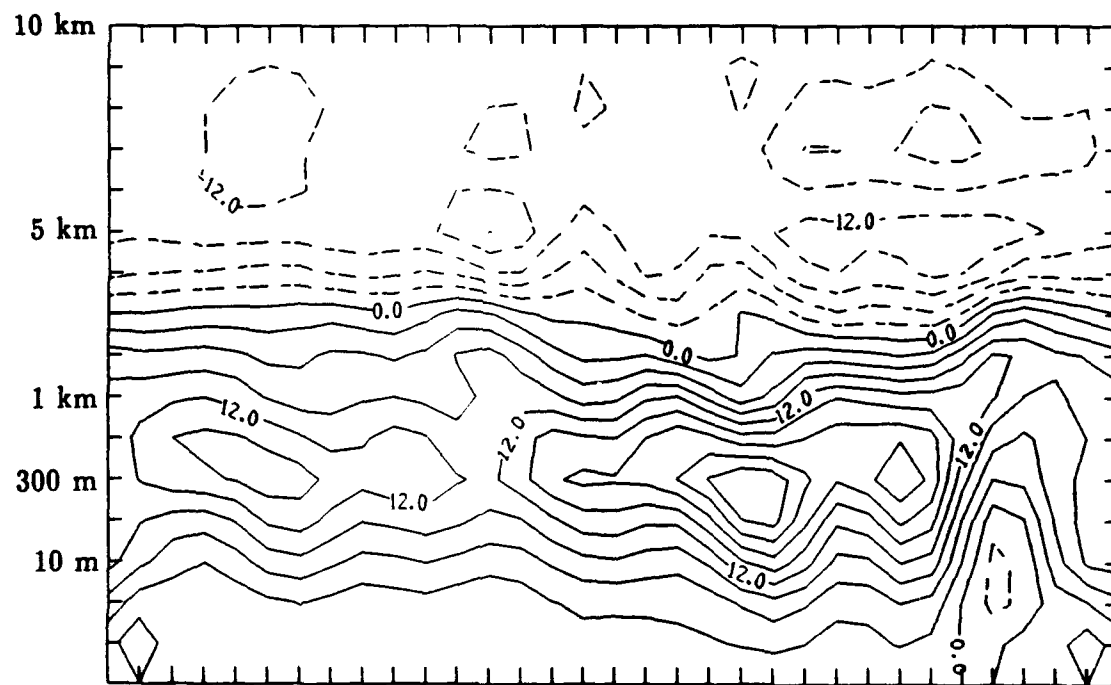


Figure 5.7. East-west vertical cross-section of forecast wind field at $J=7$. Contour interval is 3 m/sec.

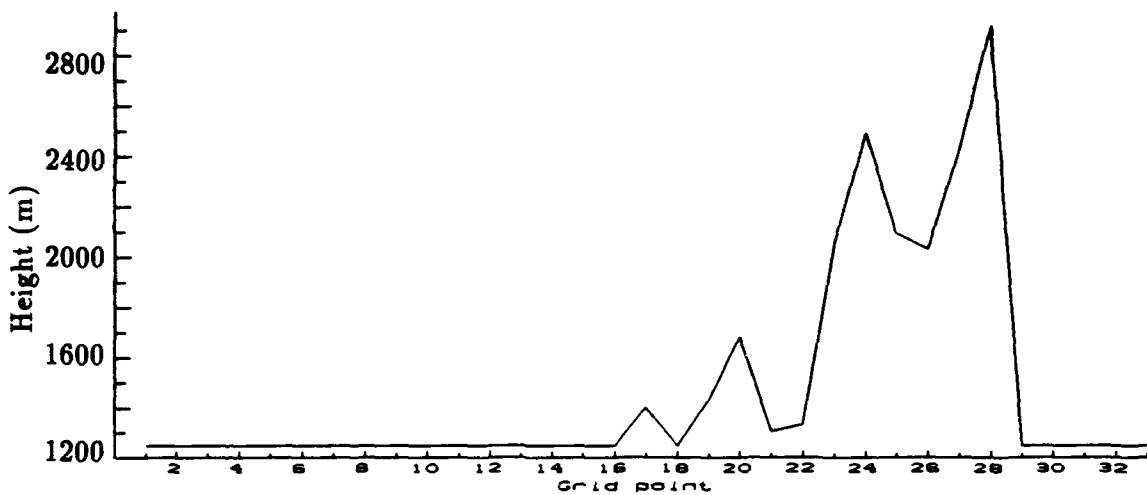


Figure 5.8. Terrain profile at $J=10$.

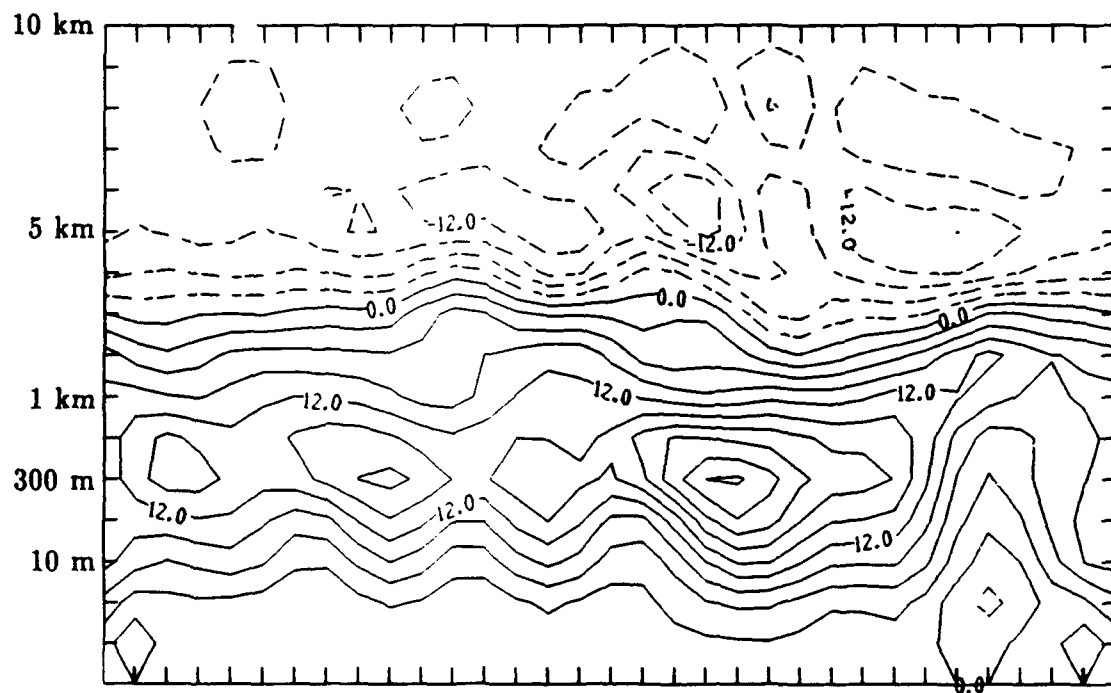


Figure 5.9. East-west vertical cross-section of forecast wind field at $J=10$. Contour interval is 3 m/sec.

wind fields are very similar at this time, although the three-dimensional run is ultimately much stronger. The results are close enough, however, to justify the conclusions reached from the two-dimensional results.

CHAPTER 6

CONCLUSIONS

Damaging windstorms occur on the lee side of all major mountain ranges and have been particularly well studied near Boulder, CO. Although previous studies have linked the vertical wind profile and stability to the development and severity of strong winds, they have used simplifications including idealized terrain, first order diagnostic equations for turbulence terms and have ignored the diurnal cycle. The purpose of this study has been to examine the influence of these variables with a relatively complete model that uses realistic topography from the Wasatch Mountains, a prognostic turbulence parameterization, and a complete diurnal cycle.

The first tests presented, in Chapter 3, were two-dimensional runs that investigated model sensitivity to lateral boundary conditions and examined the influence of the vertical mixing coefficient parameterization and the radiation calculations. These tests validated the necessity of a complex model in order to simulate development of strong downslope wind amplification for complicated topography.

Comparison of runs with a Gaussian shaped mountain in different positions within the domain showed an oscillation developing after about 8 hours caused by a reflection from the boundaries. Adding a sponge layer adjacent to each lateral boundary removed this oscillation. The sponge layer was constructed by increasing the horizontal diffusion coefficient linearly from the interior value, calculated from the grid spacing and velocity shear terms, to a boundary value, determined by the grid spacing and time step. This series of runs was done without radiation terms;

therefore, the results of an essentially constant forecast windspeed, after an initial adjustment period, tended to a steady state as expected.

The simplification of the vertical mixing coefficient to a time invariant height dependent term weakened the diurnal cycle, the maximum forecast nocturnal wind-speeds, and the atmospheric stability. Both this simplification, and the removal of the radiation calculations, significantly hindered the model's prognostic ability to simulate strong windstorm evolution as in the more complete control run.

In Chapter 4, the sensitivity of strong windstorm development to initial wind and stability profiles was investigated. Results from runs with three initial vertical wind profiles were presented. A comparison of the magnitude of the strongest low level windspeeds forecast at 18.0 hours (midnight local time) showed that the strongest wind amplification occurred with a vertical wind profile that reversed with height. The maximum wind speed for this run was 32.5 m/sec and occurred at grid point 41 and a height of 300 m.

Using the vertically reversing wind profile and adding a surface based inversion changed the maximum low level wind forecast at 18.0 hours to 30.9 m/sec at grid point 51 and a height of 300 m. With an inversion based near mountain top, the maximum windspeed forecast at 18.0 hours was 29.8 m/sec at grid point 46, at a height of 300 m. Thus the atmospheric stratification plays an important role in determining the speed and location of the maximum low level winds.

The relative magnitudes of the momentum equation terms were also studied. The Bernoulli, pressure gradient, terrain following and diffusion terms were all found to make significant contributions, with the Bernoulli and diffusion terms acting against the pressure gradient and terrain following terms in the region of interest.

In summary, the two-dimensional experiments gave results similar to those found by other investigators; namely that the vertical wind and initial stability profiles

are important in determining the amplitude of strong windstorms, and that these windstorms are localized to the region of steep terrain, with little horizontal extent. This study differed from previous studies; however, because it included a more complete turbulence treatment and diurnal cycle. These parameters were shown to be important in forecasting the magnitude and character of the resultant wind fields. The diurnal cycle of surface heating and cooling, and day to night variations of turbulent mixing, have first order effects on the local response in our interpretation. The three-dimensional results suggest that the two-dimensional case is representative of results that would be obtained from a more complete three-dimensional model, at least for the single investigated case.

Additional work is required to study why the model tends to overpredict down-slope wind maxima. We are continuing to investigate whether this is related to boundary conditions that maintain the same ambient state at both inflow and outflow boundaries. More research is also required in this area to carefully test other influences such as canyon funneling, gap winds, and other more complex windflow problems.

REFERENCES

Arakawa, S., 1969: Climatological and dynamical studies on the local strong winds, mainly in Hokkaido, Japan. *Geophys. Mag.*, **34**, 359-425.

Astling, E. G., J. Paegle, E. Miller and C. J. O'Brien, 1985: Boundary layer control of nocturnal convection associated with a synoptic scale system. *Mon. Wea. Rev.*, **113**, 540-552.

Berri, G. J., and Paegle, J., 1990: Sensitivity of local predictions to initial conditions. *J. Appl. Meteor.*, **29**, 256-267.

Blumen, W. and C. S. Hartsough, 1985: Reflection of hydrostatic gravity waves in a stratified shear flow. Part II: Application to downslope surface windstorms. *J. Atmos. Sci.*, **42**, 2319-2331.

Clark, T. L., 1977: A small-scale model using a terrain-following coordinate transformation. *J. Comput. Phys.*, **24**, 186-215.

Clark, T. L., and W. R. Peltier, 1977: On the evolution and stability of finite-amplitude mountain waves. *J. Atmos. Sci.*, **34**, 1715-1730.

— and —, 1984: Critical level reflection and the resonant growth of nonlinear mountain waves. *J. Atmos. Sci.*, **41**, 3122-3134.

Corby, G. A., 1954: The airflow over mountains. A review of the state of current knowledge. *Quart. J. Roy. Meteor. Soc.*, **80**, 491-521.

Durran, D. R. and J. B. Klemp, 1983: A compressible model for the simulation of moist mountain waves. *Mon. Wea. Rev.*, **111**, 2341-2361.

—, 1986: Another look at downslope windstorms. Part I: The development of analogs to supercritical flow in an infinitely deep, continuously stratified fluid. *J. Atmos. Sci.*, **43**, 2527-2543.

—, 1990: Mountain waves and downslope winds. *Atmospheric Processes over Complex Terrain*, W. Blumen, Ed., Amer. Meteor. Soc., 59-81.

Förchtgott, J., 1949: Wave streaming in the lee of mountain ridges. *Bull. Met. Czech.*, Prague, **3**, 49.

—, 1952: Mechanical turbulence. *Letecká Met.*, Prague, 114.

Houghton, D. D. and E. Isaacson, 1968: Mountain winds. *Stud. Num. Anal.*, **2**, 21-52.

— and A. Kasahara, 1968: Nonlinear shallow fluid flow over an isolated ridge. *Commun. Pure Appl. Math.*, **21**, 1-23.

Julian, L. T. and P. R. Julian, 1969: Boulder's winds. *Weatherwise*, **22**, 108-112.

Klemp, J. B. and D. K. Lilly, 1975: The dynamics of wave-induced downslope winds. *J. Atmos. Sci.*, **32**, 320-339.

— and —, 1978: Numerical simulations of hydrostatic mountain waves. *J. Atmos. Sci.*, **35**, 78-107.

Lilly, D. K. and E. J. Zipser, 1972: The front range windstorm of 11 January 1972 - a meteorological narrative. *Weatherwise*, **25**, 56-63.

— and J. B. Klemp, 1979: The effects of terrain shape on nonlinear hydrostatic mountain waves. *J. Fluid Mech.*, **95**, 241-261.

— and —, 1980: Comments on the evolution and stability of finite-amplitude mountain waves. Part II: Surface wave drag and severe downslope windstorms. *J. Atmos. Sci.*, **37**, 2119-2121.

Long, R. R., 1953: Some aspects of the flow of stratified fluids. I. A theoretical investigation. *Tellus*, **5**, 42-58.

—, 1955: Some aspects of the flow of stratified fluids. III. Continuous density gradients. *Tellus*, **7**, 341-357.

McCorcle, M. D., 1986: The effect of soil moisture and ambient conditions on the Great Plains boundary layer. Doctoral dissertation, University of Utah, 161 pp.

Paegle, J. and D. W. McLawhorn, 1983: Numerical modeling of diurnal convergence oscillations above sloping terrain. *Mon. Wea. Rev.*, **111**, 67-85.

—, J. N. Paegle, M. McCorcle and E. Miller, 1984: Diagnoses and numerical simulation of a low-level jet during ALPEX. *Beitr. Phys. Atmos.*, **57**, 419-430.

— and T. Vukicevic, 1987: On the predictability of low-level flow during ALPEX. *Meteorol. Atmos. Phys.*, **36**, 45-60.

—, 1989: A variable resolution global model based upon Fourier and finite element representation. *Mon. Wea. Rev.*, **117**, 583-606.

Peltier, W. R. and T. L. Clark, 1979: The evolution and stability of finite-amplitude mountain waves. Part II: Surface wave drag and severe downslope winds. *J. Atmos. Sci.*, **36**, 1498-1529.

— and —, 1980: Reply. *J. Atmos. Sci.*, **37**, 2122-2125.

—, and J. F. Scinocca, 1990: The origin of severe downslope windstorm pulsations. *J. Atmos. Sci.*, **47**, 2853-2870.

Queney, P., 1947: Theory of perturbations in stratified currents with application to airflow over mountain barriers. University of Chicago Report No. 23, Dept. of Meteorology, University of Chicago Press.

Scinocca, J. F. and W. R. Peltier, 1989: Pulsating downslope windstorms. *J. Atmos. Sci.*, **46**, 2885-2914.

Scorer, R. S., 1949: Theory of waves in the lee of mountains. *Quart. J. Roy. Meteor. Soc.*, **75**, 41-56.

—, 1953: Theory of airflow over mountains: II - The flow over a ridge. *Quart. J. Roy. Meteor. Soc.*, **79**, 70.

—, 1954: Theory of airflow over mountains: III - Airstream characteristics. *Quart. J. Roy. Meteor. Soc.*, **80**, 417.

—, and H. Klieforth, 1959: Theory of mountain waves of large amplitude. *Quart. J. Roy. Meteor. Soc.*, **85**, 131-143.

Smith, R.B., 1977: The steepening of hydrostatic mountain waves. *J. Atmos. Sci.*, **34**, 1634-1654.

—, 1985: On severe downslope winds. *J. Atmos. Sci.*, **42**, 2597-2603.

—, 1987: Aerial observations of the Yugoslavian Bora. *J. Atmos. Sci.*, **44**, 269-297.

Yamada, T., and S. Bunker, 1989: A numerical model study of nocturnal drainage flows with strong wind and temperature gradients. *J. Appl. Meteor.*, **28**, 545-554.

Zdunkowski, W. G., R. M. Welch and J. Paegle, 1976: One-dimensional numerical simulation of the effects of air pollution on the planetary boundary layer. *J. Atmos. Sci.*, **33**, 2399-2414.